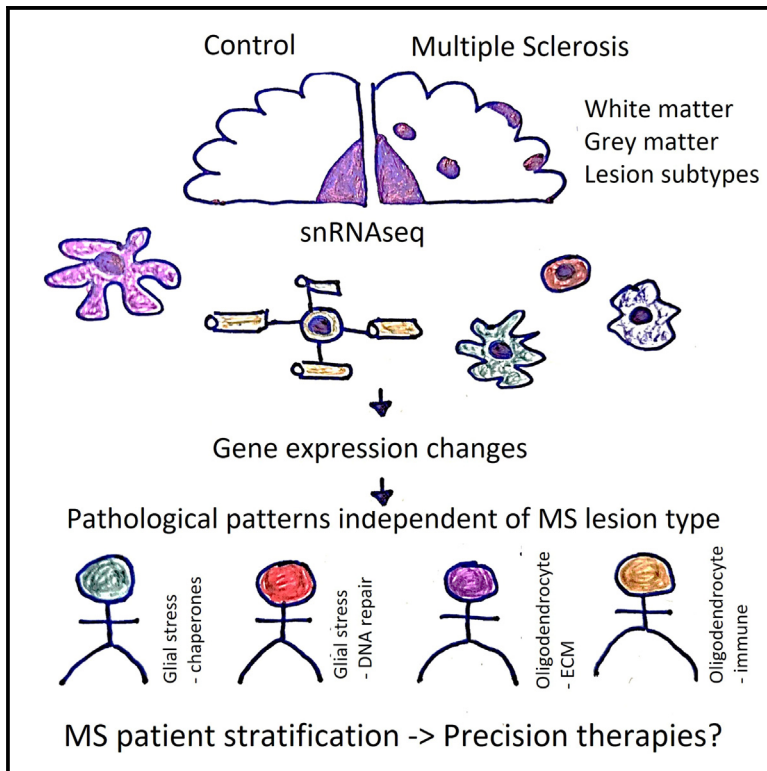


snRNA-seq stratifies multiple sclerosis patients into distinct white matter glial responses

Graphical abstract



Authors

Will Macnair, Daniela Calini, ...,
Charles French-Constant,
Gonçalo Castelo-Branco,
Anna Williams, Dheeraj Malhotra

Correspondence

will.macnair@roche.com (W.M.),
cffc@uea.ac.uk (C.f.-C.),
goncalo.castelo-branco@ki.se (G.C.-B.),
anna.williams@ed.ac.uk (A.W.),
dheeraj21malhotra@gmail.com (D.M.)

In brief

Macnair and Calini et al. analyze 632,000 snRNA-seq profiles from multiple sclerosis and control brain samples, identifying distinct cellular responses in white and gray matter. They stratify MS patients into groups based on patterns of gene expression in white matter glia, suggesting different pathological processes and future personalized therapies.

Highlights

- snRNA-seq atlas of multiple sclerosis brain white and gray matter versus control
- Patient-specific glial gene expression patterns stratify MS patients
- Findings support precision medicine approaches for MS

Article

snRNA-seq stratifies multiple sclerosis patients into distinct white matter glial responses

Will Macnair,^{1,12,*} Daniela Calini,^{1,12} Eneritz Agirre,^{2,13} Julien Bryois,^{1,13} Sarah Jäkel,^{3,4,13} Rebecca Sherrard Smith,¹⁰ Petra Kukanja,² Nadine Stokar-Regenscheit,⁵ Virginie Ott,⁵ Lynette C. Foo,¹ Ludovic Collin,¹ Sven Schippling,¹ Eduard Urich,¹ Erik Nutma,⁶ Manuel Marzin,⁶ Federico Ansaloni,² Sandra Amor,⁶ Roberta Magliozzi,⁷ Elyas Heidari,⁸ Mark D. Robinson,⁸ Charles French-Constant,^{9,14,15,*} Gonçalo Castelo-Branco,^{2,14,15,*} Anna Williams,^{10,14,15,16,*} and Dheeraj Malhotra^{1,11,14,15,*}

¹Roche Pharma Research and Early Development, Neuroscience and Rare Diseases, Roche Innovation Center, Basel, Switzerland

²Laboratory of Molecular Neurobiology, Department of Medical Biochemistry and Biophysics, Karolinska Institutet, 17177 Stockholm, Sweden

³Institute for Stroke and Dementia Research (ISD), Klinikum der Universität München, Ludwig-Maximilians Universität, Munich, Germany

⁴Munich Cluster of Systems Neurology (SyNergy), Munich, Germany

⁵Roche Pharma Research and Early Development (pRED), Pharmaceutical Sciences, Pathology and Applied Safety Sciences, Roche Innovation Center Basel, F. Hoffmann-La Roche Ltd., Grenzacherstrasse 124, 4070 Basel, Switzerland

⁶Department of Neurobiology and Aging, Biomedical Primate Research Centre, Rijswijk, the Netherlands

⁷Department of Neurosciences, Biomedicine and Movement Sciences, University of Verona, Verona, Italy

⁸Department of Molecular Life Sciences and SIB Swiss Institute of Bioinformatics, University of Zurich, Winterthurerstrasse 190, 8057 Zurich, Switzerland

⁹Faculty of Medicine and Health Sciences, University of East Anglia, Norwich Research Park, Norwich NR4 7TJ, UK

¹⁰Centre for Regenerative Medicine, Institute for Regeneration and Repair, MS Society Edinburgh Centre for MS Research, The University of Edinburgh, 5 Little France Drive, Edinburgh EH16 4UU, UK

¹¹Present address: MS Research Unit, Biogen, Cambridge, MA 02142, USA

¹²These authors contributed equally

¹³These authors contributed equally

¹⁴These authors contributed equally

¹⁵Senior author

¹⁶Lead contact

*Correspondence: will.macnair@roche.com (W.M.), cffc@uea.ac.uk (C.f.-C.), goncalo.castelo-branco@ki.se (G.C.-B.), anna.williams@ed.ac.uk (A.W.), dheeraj21malhotra@gmail.com (D.M.)
<https://doi.org/10.1016/j.neuron.2024.11.016>

SUMMARY

Poor understanding of the cellular and molecular basis of clinical and genetic heterogeneity in progressive multiple sclerosis (MS) has hindered the search for new effective therapies. To address this gap, we analyzed 632,000 single-nucleus RNA sequencing profiles from 156 brain tissue samples of MS and control donors to examine inter- and intra-donor heterogeneity. We found distinct cell type-specific gene expression changes between MS gray and white matter, highlighting clear pathology differences. MS lesion subtypes had different cellular compositions but surprisingly similar cell-type gene expression patterns both within and across patients, suggesting global changes. Most gene expression variability was instead explained by patient effects, allowing us to stratify patients and describe the different pathological processes occurring between patient subgroups. Future mapping of these brain molecular profiles with blood and/or CSF profiles from living MS patients will allow precision medicine approaches anchored in patient-specific pathological processes.

INTRODUCTION

Although we have highly effective therapies for the early inflammatory relapsing-remitting phase of multiple sclerosis (MS), we lack such therapies for the neurodegenerative progressive phase. Therapeutic strategies that have been tested in clinical trials include enhancing neuroprotection directly and enhancing

remyelination, resulting in indirect neuroprotection by restoring metabolic support and saltatory conduction to the demyelinated axon.¹ However, in spite of promising preclinical data, such trials have not so far resulted in improvement in clinical disability, even though subgroup analysis has shown some promise (e.g., MS-SMART,² Opicinumab,³ Bexarotene,^{4,5} and Clemastine⁶). This translational mismatch may result from the diversity of disease

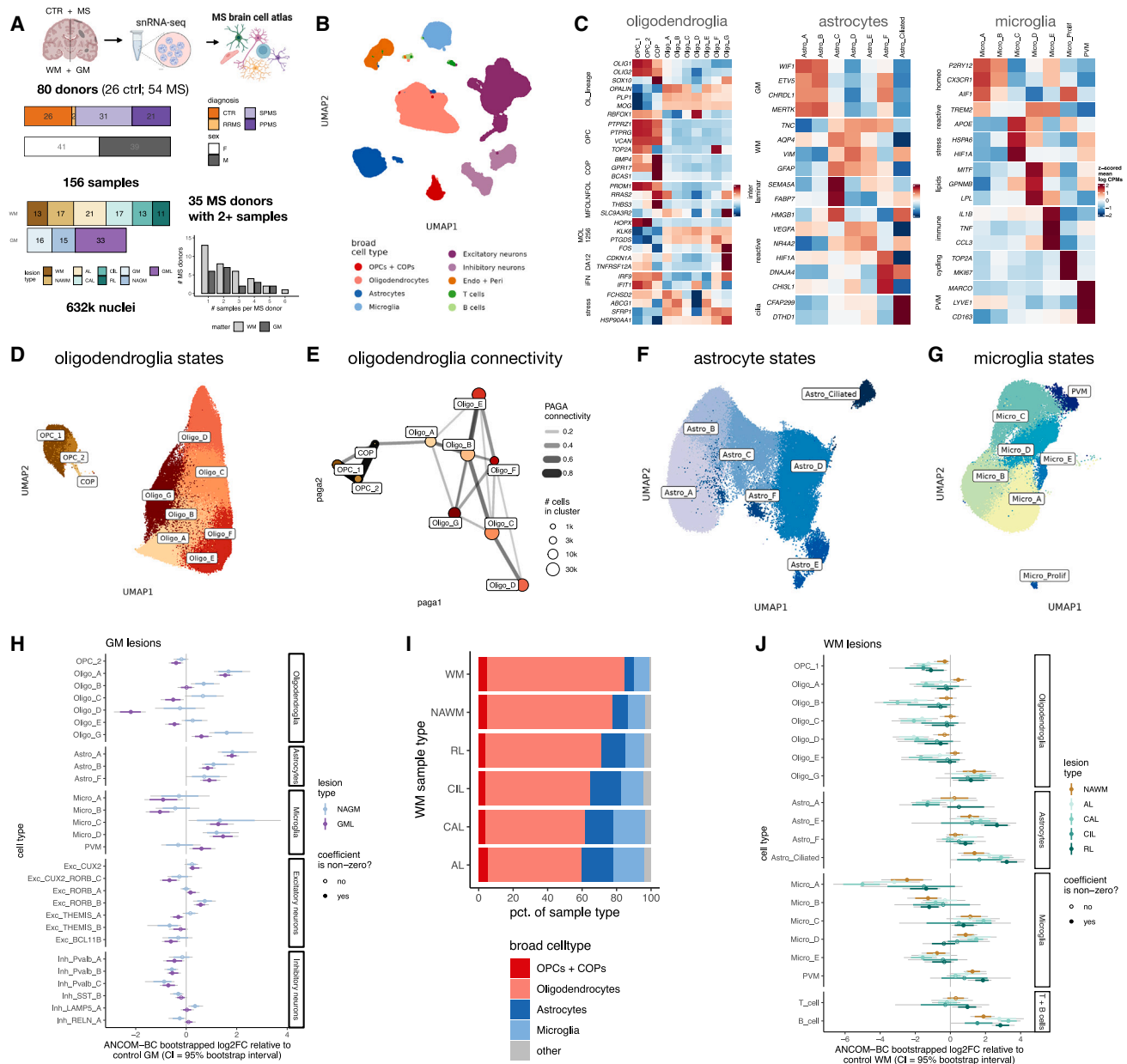


Figure 1. Single-cell dissection of cellular heterogeneity in multiple sclerosis lesions

(A) Overview of the donor and sample characteristics (CTRL, control; RRMS, relapsing-remitting MS; SPMS, secondary progressive MS; PPMS, primary progressive MS).

(B) Uniform manifold approximation and projection (UMAP) plot of cell types. (Endo + Peri, endothelial cells and pericytes).

(C) Heatmaps showing selected markers of glial states and their subclusters. Color shows Z scored mean log CPMs, scaled per gene across glial states. Oligodendroglia: OPC, oligodendrocyte precursor cell; COP, committed oligodendrocyte precursor; NFOL, newly formed oligodendrocyte; MFOL, myelin forming oligodendrocyte; MOL, myelinating oligodendrocyte; DA, disease associated; IFN, interferon signaling related; gene groupings derived from Falcão et al.¹⁰ and Hilscher et al.¹¹ Astrocytes: interlaminar, interlaminar astrocytes; cilia, ciliated astrocytes and ependymal cells. Microglia: homeo, homeostatic; PVM, perivascular macrophage.

(D) UMAP plot restricted to oligodendroglia showing subclusters.

(E) PAGA applied to oligodendrocyte and OPC/COP subclusters across all samples (edges with weights below 0.2 not shown).

(F) UMAP plot restricted to astrocytes showing subclusters.

(G) UMAP plot restricted to microglia showing subclusters.

(H) Differential abundance of GM MS samples against control GM, as calculated by bootstrapped Analysis of Compositions of Microbiomes with Bias Correction (ANCOM-BC) (see STAR Methods and supplemental information). The model accounts for sample layer position, by using formula $count \sim lesion_type + sex + age_scale + pmi_cat + layer_PC1 + layer_PC2 + layer_PC3 + layer_PC4$ (where *age_scale* is age at death, normalized to have SD = 0.5¹²). The line at

(legend continued on next page)

response in people with MS: within both primary and secondary progressive MS (PPMS and SPMS) clinical subtypes, there is a clear heterogeneity of clinical course, with some people with MS never reaching the progressive disability phase, while others rapidly become disabled. This diverse disease course is difficult to predict at disease onset in the individual, either using patient characteristics or currently available imaging/biomarker tools. We speculated that these differing disease outcomes relate to a heterogeneous neurodegenerative and/or neuroregenerative MS pathological response between patients. In previous work, we and others identified cellular heterogeneity in MS using single-nucleus transcriptomics, albeit in a limited number of patients and pathological MS lesion types.^{7–9} However, these studies had insufficient samples to characterize inter-patient or intra-patient heterogeneity. To address this critical gap, we performed a single-nucleus RNA sequencing (snRNA-seq) study on the most extensive cohort of MS patients to date (Figure 1A), including both white matter (WM) and gray matter (GM) areas. Our goals were first to identify the basis of heterogeneity by comparing cellular compositions and cell type-specific gene expression signatures across WM and GM MS lesion types. Second, we sought to identify pathologically relevant ways of stratifying patients on the basis of these responses, to better find and test potential therapies for progressive MS.

RESULTS

Diverse neural cell subtypes observed in brain WM and GM in MS and controls

We profiled 173 WM and GM samples, including >950,000 nuclei from 55 MS cases and 30 controls (pre QC), and >630,000 nuclei from 54 MS cases and 28 controls (post QC). Our cohort was similar for age, gender, and post-mortem interval (PMI) between MS and controls (Figures S1A and S1B; Data S1 and S2; Table S1). After randomization of samples during library preparation and sequencing to minimize batch effects, followed by doublet removal and cell and sample QC, including using CellBender¹³ to reduce ambient RNA (STAR Methods), we obtained 632,375 single-nucleus transcriptomes from 156 QC-passed samples, including 506,594 nuclei from MS patients and 125,781 nuclei from controls, profiled at a median depth of 3,810 nuclei/sample, 3,508 reads/nucleus, and 1,826 genes/nucleus (Data S1 and S2). These comprised 62 WM lesions (WMLs) (21 active demyelinated lesions [AL], 17 chronic active demyelinated lesions [CAL], 13 chronic inactive demyelinated lesions [CIL], and 11 remyelinated lesions [RL]), 17 adjacent normal-appearing WM (NAWM) regions from MS patients, and 13 cortical hemisphere WM regions from non-neurological controls. In addition, we profiled 33 subpial cortical GM demyelinated lesions (GMLs), 15 adjacent normal-appearing GM (NAGM) regions

from MS patients, and 16 cortical GM tissues from controls, all defined per classical neuropathology,¹⁴ thereby creating a comprehensive atlas of single-nuclei MS transcriptomes (Figure 1A). We performed pre-processing, integration, and clustering via two distinct pipelines (STAR Methods; integration performed with Harmony^{15,16} and Conos¹⁷), and the clusters identified showed high agreement (Data S1 and S3). All clusters had acceptable QC metrics, and no cluster was composed of nuclei captured only from individual patients, samples, lesion types, or technical covariates, indicating that data integration was successful (Data S1). This captured all major cell types of the human cortical GM and WM (Figure 1B) identified using canonical markers (Figures 1C and S2), derived from both MS and control donor samples (Data S1). There was regional and disease-related heterogeneity, and we found 59 distinct fine cell type clusters (STAR Methods), including 14 subtypes of cortical excitatory neurons (across layers 2–6), 12 of inhibitory neurons, 10 of oligodendroglia, 7 of astrocytes, 7 of microglia/macrophages, 7 blood vessel-related cells (including 4 endothelial cell and 1 pericyte clusters), and B cell and T cell subpopulations (Figure S2; Data S4). We also identified 9 small clusters with mixed lineages, which were potentially doublets (Figure S2; Data S1 and S4) and were not considered further.

We interrogated the fine cell type clusters in turn. Based on the expression of previously described genes characterizing oligodendroglia,^{7,10,18} we identified 2 oligodendrocyte precursor cell (OPC, *OLIG1+*, *PTPRG+*, *PTPRZ1+*), 1 committed oligodendrocyte precursor (COP, *GPR17+*, *BCAS1+*), and 7 oligodendrocyte populations (Figures 1C and 1D; Data S4). (Example of GPR17 validation for COPs shown in Figure S3). Analysis of connectivity with partition-based graph abstraction (PAGA)¹⁹ found a putative main trajectory from OPCs to COPs, followed by Oligo_A, then Oligo_B to C, and finally Oligo_D (Figure 1E). Markers of this pathway were suggestive of classical oligodendrocyte differentiation, leading from Oligo_A immature markers (e.g., *OPALIN*, *PLP1+*), through B and C, to Oligo_D oligodendrocytes with most myelin protein transcripts (e.g., *MOG+* along with *RBFOX1* and *KLK6*) (Figures 1C and 1E; Data S4). However, there is, in both MS WM and control WM, an additional branch point to the large cluster Oligo_E, expressing immature markers as well as transcripts relating to cell morphology, cholesterol synthesis, and active metabolism (e.g., *FCHSD2*, *ABCG1*,²⁰ *SFRP1*) (Data S4). We also found 2 additional branches leading to either Oligo_F or G, both of which are disease-associated (DA) (see below), expressing transcripts related to the interferon response (e.g., *IRF9*) (Figure 1C). Oligo_G expresses transcripts related to heat shock protein and chaperone protein folding responses (e.g., *HSP90AA1*) and *CDKN1A* and *TNFRSF12A*, similar to the DA2 clusters described in mice²¹ (Figure 1C; Data S4). Oligo_F expresses

0 corresponds to no difference between healthy and MS. Points correspond to median log₂FC effect estimated by ANCOM-BC; colored range is 80% bootstrapped confidence interval, the gray range is 95% confidence interval (CI). Points are filled when the 95% CI excludes zero; otherwise, empty.

(I) Pseudobulk analysis showing percentage (pct) of broad cell types in each sample group.

(J) Differential abundance of WM MS samples against control WM, as calculated by bootstrapped ANCOM-BC as in (H). Model fitted is $count \sim lesion_type + sex + age_scale + pmi_cat$. Abbreviations: WM, white matter; GM, gray matter; NAWM, normal-appearing white matter; NAGM, normal-appearing gray matter; AL, active demyelinated lesion; CAL, chronic active demyelinated lesion; CIL, chronic inactive demyelinated lesion; RL, remyelinated lesion; GML, gray matter demyelinated lesion.

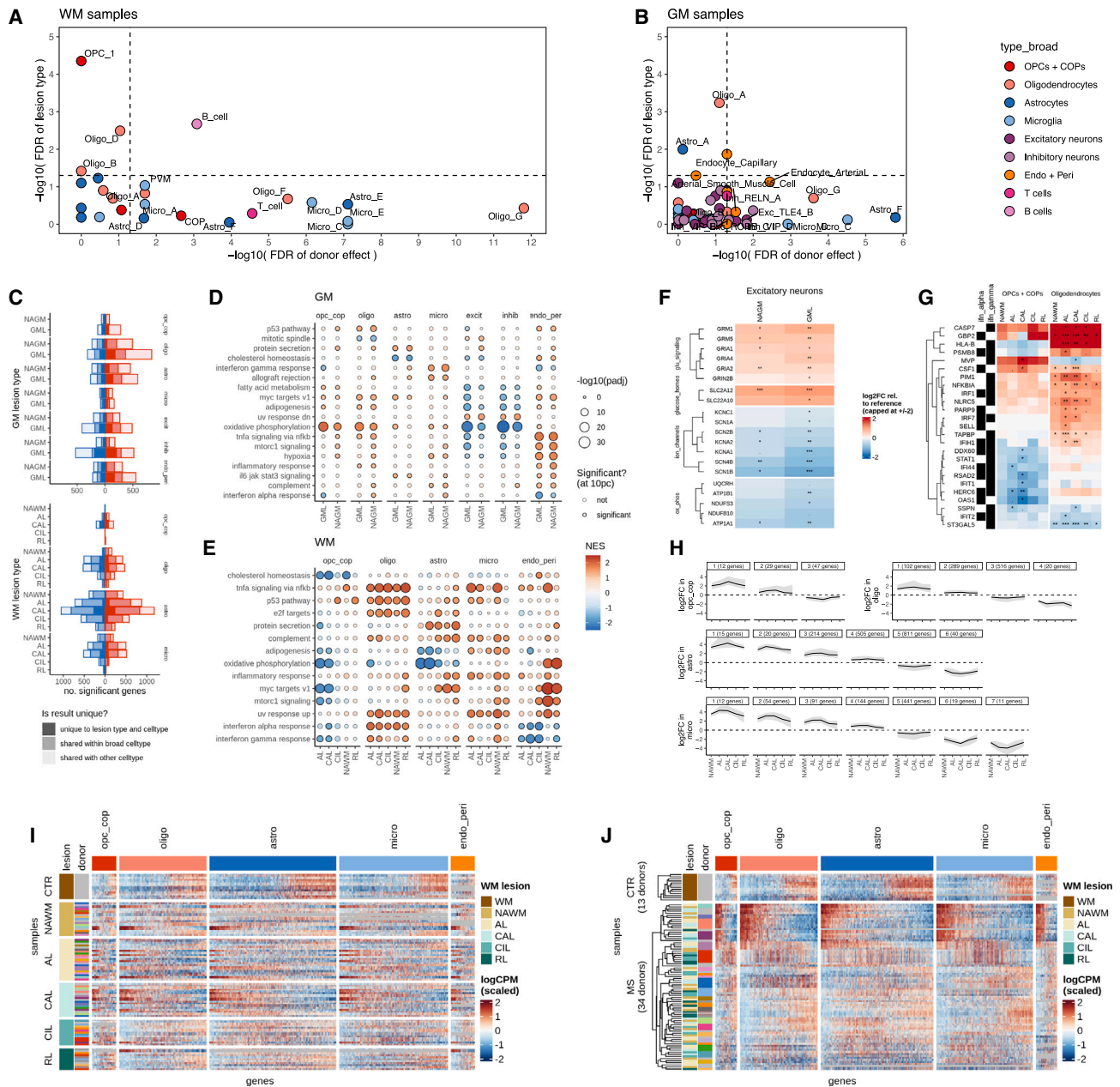


Figure 2. Patterns and determinants of cell type-specific gene expression profiles in WMLs and GMLs

(A and B) Contribution to variability in cell type abundances explained by lesion plus patient in WM (A) and GM (B). In (B), three neuronal layer PCs are included as confounders. FDR is Benjamini-Hochberg-corrected p values from likelihood ratio tests of nested models. Axes show evidence that lesion type (y axis) or donor effect (x axis) significantly improve the fit of a model explaining the cell type proportion of a sample.

(C) Bar charts showing number of significant differentially expressed (DE) genes for WM and GM tissue and cell type, only DE for this cell type, or also DE in another cell type.

(D and E) Dot plots of top GO terms plotted for broad cell types and tissue (GM, D; WM, E). Key is shared.

(F) DE genes related to glutamate signaling, glucose homeostasis, ion channels, and oxidative phosphorylation in excitatory neurons in GMLs (mean \log_2 CPM).

(G) Differential expression of interferon alpha and gamma genes in oligodendroglial cells in WMLs (mean \log_2 CPM).

(H) WM gene expression fold change profiles over lesion types for each broad cell type showing continuous patterns (opc_cop, OPCs + COPs; oligo, oligodendrocytes; astro, astrocytes; micro, microglia). Restricted to genes where at least one lesion type has FDR < 15%, hierarchical clustering with cut distance set to $\log(4)$, and clusters with fewer than 10 genes not shown. The figure in brackets shows the number of genes in the cluster.

(I) Pseudobulk expression heatmap of genes showing either MS or donor variability in broad cell types in WM, samples ordered by lesion type.

(J) Pseudobulk expression heatmap as in (I), row order on the basis of hierarchical clustering, showing differences between MS donors not explained by lesion type, sex, or type of MS, but all samples from one donor cluster together, suggesting a strong donor effect.

(legend continued on next page)

transcripts related to DNA damage and injury (e.g., *TOP2A*) (Data S4).

Astrocytes (Figure 1F) were divided into GM and WM types, expressing *WIF1*, *ETV5* (GM, Astro_A–B) and *TNC* (WM, Astro_D–F), similar to those in mice²² (Figure 1C). GM astrocytes are more involved in synapse function (e.g., *CHRD1*) and phagocytosis (e.g., *MERTK*), whereas WM astrocytes are more involved with blood-brain barrier (BBB) function and water transport (e.g., with higher expression of *AQP4*) (Figure 1C; Data S4). Astro_D–F are more reactive, expressing higher levels of *VEGFA*, *HIF1A*, or *CHI3L1* (Figure 1C). A clear cluster of ciliated astrocytes was present (*CFAP299*, *DTHD1*) (Figures 1C and 1F).

Similar to signatures identified in recent microglial datasets,²³ we observed microglial subclusters expressing transcripts associated with homeostasis, in addition to more reactive subclusters (Figures 1C and 1G). Micro_A and Micro_B appear to be homeostatic, showing relatively high expression of *P2RY12* and *CXCR1*, while Micro_C–E had a more reactive phenotype, expressing higher levels of transcripts such as *TREM2* and *APOE* (Figure 1C; Data S4). Some microglia expressing these markers have been described in other neurodegenerative diseases in mice and humans, sometimes termed DA microglia (DAM) or microglia inflamed in MS (MIMS).²³ Micro_C expresses markers related to stress and chaperone proteins (e.g., *HSPA6*, *HIF1A*), Micro_D markers such as *GNMB* and *MITF*, and Micro_E markers such as *IL1B* and *CCL3*. Perivascular macrophages (PVMs)/border-associated macrophages were also detected, expressing high levels of transcripts such as *MARCO* and *LYVE1* (Figures 1C and 1G).

Neuronal heterogeneity reflected the subtypes of excitatory and inhibitory neurons found in cortical layers in human GM, including for excitatory neurons, *CUX2*+ neurons from layer 2, *RORB*+ neurons from layer 3 and 5, and *TLE4*+ neurons in the lower layers (5/6) (Figure S2). Inhibitory GABAergic neurons subdivided by location (e.g., *RELN*+ neurons [layer 1]) and by neurotransmitter (e.g., *PVALB*+, *SST*+, *VIP*+ neurons) (Figure S2).

As a result, our dataset, which uses snRNA-seq to study the largest cohort of MS patients and lesions to date, describes a wide range of homeostatic and DA cell states. We further examined these in terms of their composition and transcriptional changes in both lesions and patients.

Distinct compositional profiles in WMLs and GMLs

Having defined our cell-type subclusters, we next investigated the compositional differences between MS and control samples. We focused first on GM samples, as we and others have shown a loss of *PVALB*+ and *SST*+ inhibitory neurons in MS GM,^{24,25} as well as a loss of some types of excitatory neurons.⁸ We reproduced these findings (Figure 1H), with effects similar between GMLs and NAGM, as before, but more pronounced in GMLs. Consistent with astrogliosis, GM astrocyte clusters Astro_A, Astro_B, and Astro_F are increased in MS in GM, both in NAGM and GMLs (Figure 1H). As expected, oligodendrocyte clusters Oli-

go_C and Oligo_D (expressing most myelin protein transcripts) are reduced in GMLs compared to NAGM and control. However, DA oligodendrocytes (Oligo_G) are increased. Immature oligodendrocytes (e.g., Oligo_A) are increased in abundance in GMLs and NAGM, and there is increased Oligo_B and Oligo_C abundance in NAGM (but not GMLs), consistent with the described regenerative response to demyelination in GMLs, which is generated in surrounding NAGM tissue and is more successful than in WM²⁶ (Figure 1H).

Turning to WM, classical pathology descriptions divide WM MS demyelinated lesions by the pattern of immune infiltrate into AL, CAL, and CIL, with additional RL (definitions in STAR Methods and Figure S4). Analysis of sample compositions at the broad cell type level confirmed the changes in overall neuronal and glial numbers previously described within the classical lesion subtypes: the expected reduction in oligodendrocytes in MS, most pronounced in demyelinated lesions; an increase in microglia/macrophages, especially in AL and CAL (defining these lesions); and an increase in astrocytes in MS compared to NAWM and control WM (Figure 1I). However, more detailed differential abundance analysis at the cell type subcluster level reveals additional differences in subcluster patterns (Figure 1J). While most oligodendrocyte subtypes were reduced in MS WM, there was an increase in immature oligodendrocyte type Oligo_A confined to NAWM, (whereas this was increased in both NAGM and GMLs, reiterating the different environments of GM and WM for oligodendrocyte regeneration), and an increase in Oligo_G (DA oligodendrocytes). There was also a change in microglia from a more homeostatic phenotype (Micro_A,B) to a more reactive type (Micro_C,D), a change of astrocytes from a more homeostatic phenotype (Astro_A) to a more reactive phenotype (Astro_E,F), and an increase in ciliated astrocytes (Astro_Ciliated) (Figure 1J). These differences were generally present in most MS samples compared to controls, but also with clear differences between MS sample types, with NAWM samples being more similar to RLs and controls, and AL and CAL being similar but with the biggest differences relative to non-MS samples. Repeat analysis with the orthogonal technique Milo²⁷ showed broadly similar results (Figures S5A and S5B).

Distinct cell type-specific transcriptional responses in GMLs and WMLs

The cell composition analysis indicates that there is considerable variation in specific glial cell types in WML and GML samples (Figures 1H–1J, 2A, and 2B). Comparing gene expression, we also found significant differences in many glial types in WM samples from different donors (12 out of 23 glia types; false discovery rate [FDR] < 0.05 for donor effect) (Figure 2A), and some in GM samples (5 out of 17; FDR < 0.05 for donor effect) (Figure 2B). To explore this further, we investigated the differential gene expression (DEG) between cells in different lesion environments, taking into account donor variation. We identified gene expression changes for each broad cell type between WMLs and control

(I and J) Column order determined by the first principal component of the gene matrix for each cell type. Abbreviations: WM, white matter; GM, gray matter; NAWM, normal-appearing white matter; NAGM, normal-appearing gray matter; AL, active demyelinated lesion; CAL, chronic active demyelinated lesion; CIL, chronic inactive demyelinated lesion, RL, remyelinated lesion; GML, gray matter demyelinated lesion; opc_cop, OPCs and COPs; oligo, oligodendrocytes; astro, astrocytes; micro, microglia; endo_peri, endothelial cells + pericytes.

WM tissue, and between GMLs and control GM tissue using a mixed model (glmmTMB²⁸) fit to pseudobulk data, including age, sex, and PMI as possible confounding variables, and donor ID as a random component (STAR Methods; supplemental information). Indeed, the fitted models for all broad cell types showed strong donor effects for many genes (Figures S6A and S6B). Nevertheless, we identified 5,106 DEGs in WM and 4,824 DEGs in GM across all major cell types (Figure 2C; Data S5; https://malhotralab.shinyapps.io/MS_broad/).

To identify signatures of the different WML types described in many previous classical MS pathology studies, we next compared “bulk-like” transcriptional changes between control and different MS WM samples and found many genes were transcriptionally regulated, with the most numerous changes in AL and CAL (Figure S7). Of the many genes of interest, we highlight one example, *S1PR3*, which is increased in expression in AL and CAL, and described previously as increased at the protein level in “active MS lesions.”²⁹ With snRNA-seq, we can identify that *S1PR3* is mainly expressed in vascular cells and astrocytes (https://malhotralab.shinyapps.io/MS_broad/), and this is of interest as S1PRs are the targets of the S1PR modulator family of MS disease-modifying drugs such as fingolimod, ozanimod, ponesimod, and siponimod—the last of which is licensed for use in SPMS.

Examining the snRNA-seq profiles, all cell types in MS GM and WM showed strong changes in gene expression, more marked in demyelinated lesions than normal-appearing matter (Figure 2C), with gene ontology analysis (Figures 2D and 2E) indicating several altered pathways. In GM, both excitatory and inhibitory neurons showed more DEGs in GMLs compared to NAGM, predominantly in selectively vulnerable neuronal cells (*PVALB*+ interneurons and upper/mid layer excitatory neurons) (Data S5; https://malhotralab.shinyapps.io/MS_fine/). Focusing on MS excitatory neurons (residing in layer II/IV), there was upregulation of genes related to glutamate signaling (e.g., *GRIA1,2,4*, *GRIN2B*, *GRM1,5*), glucose or cation homeostasis (*SLC2A12*, *SLC22A10*) with concurrent downregulation of specific ion channels (*SCN1A*, *SCN1B*, *SCN2B*, *SCN4B*, *KCNA1*, *KCNA2*, *KCNC1*) and oxidative phosphorylation (OXPHOS) genes (*ATP1A1*, *ATP1B1*, *NDUFB10*, *NDUFS3*, *UQCRRH*) (Figure 2F). This unregulated glutamate signaling in excitatory neurons, together with the decrease in inhibitory neurons (Figure 1H), could potentially generate excitotoxicity that would contribute to MS GM pathology.

In WMLs, consistent with our prior observations,^{10,30} expression of genes involved in interferon alpha and gamma responses varied across MS lesions and often showed opposite patterns in OPCs compared to oligodendrocytes (Figure 2G). Genes involved in inflammation-related pathways were also enhanced in astrocytes, microglia, and oligodendrocytes in WMLs (Figure 2E). However, at the snRNA-seq level, we found no patterns of gene expression predictive of lesion type. Within each glial broad type, the majority of DEGs were shared across lesions (Figures 2E and 2G). For some such transcripts, we observed “u”/“n”-shaped profiles of transcriptional changes along the pathological category of the lesion, with NAWM lesions showing small fold changes relative to control WM, increasing to the largest fold changes in AL and CAL, then decreasing again in

CIL and RL (Figure 2H; STAR Methods). This indicated that there is a continuum of transcriptional differences across MS lesions, most likely reflecting global neuropathology.

Donor effects drive cellular and transcriptional heterogeneity in MS brains

The cell-type abundance and gene expression comparisons show distinct changes associated with MS, with a continuum of cellular (Figures 1H and 1J) and transcriptional pathology across lesion categories, which does not fully explain the differences in our data (Figures 2D–2H). Based on the significant inter-individual variation in cell type gene expression noted above, we hypothesized that different subgroups of patients might better share transcriptional pathological signatures than lesion types. This hypothesis could not be explored in prior bulk RNA-seq studies of WMLs, but the unique strength of our study design, with multiple different lesion types from the same patient and the power of single-nuclei resolution, enables it to be tested.

For each sample, and in each broad cell type, we analyzed the gene expression pattern for genes that either showed significant disease effect or were highly variable for each sample. As expected from our earlier results, there was no pattern of upregulation or downregulation of genes that correlated with sample neuropathological category or lesion type, in either WMLs (Figure 2I) or GMLs (Figure S8A). However, in both WM and GM samples, hierarchical clustering of the same data showed a clear expression pattern that correlated with the donor ID of the samples (Figures 2J and S8B). This provided strong evidence for cross-cell type transcriptional similarity within patients. Within an individual patient, the gene expression profiles were remarkably similar across multiple lesion types and normal-appearing matter, while subgroups of different patients showed distinct transcriptional profiles (Figures 2I, 2J, S8A, and S8B). We concluded that although MS lesions clearly differed in cellular composition, at the gene expression level, cells within both WMLs and GMLs appeared more affected by donor identity rather than by the lesion environment.

Coordinated multicellular gene expression programs define patient subgroups

This demonstration that patients with long-standing MS differ markedly in the transcriptional signatures of their glia, whatever their lesion classification, yet fall into apparent subgroups, is important in the context of the variable responses to experimental neuroprotective therapies, such as those targeting remyelination. To explore these apparent subgroups more, and to understand the underlying cellular and molecular mechanisms, we adapted multiomics factor analysis (MOFA) to identify similar donor-associated transcriptional patterns across multiple cell types (modalities) simultaneously.^{31,32} For each cell type, we selected genes with evidence of an MS effect and/or a donor effect (Figures S6A and S6B) to capture both consistent MS pathology and patient-patient variability. This resulted in gene sets largely distinct for each cell type, with some common genes (Figures S9A and S9B). MOFA identified five factors each in both GM (GM_F1-5) and WM (WM_F1-5) samples that explained at least 5% of variability for a cell type, with each factor describing one axis of variation in MS. Where the factor explains variance in

multiple cell types simultaneously, this represents a cross-cellular response to MS; where the factor explains variance mostly in one cell type, this program is most influential in that cell type.

In GM samples, for all factors except factors GM_F1 and GM_F3, there was considerable overlap between the distributions of control and MS samples (Figure S10A). Factor GM_F1 gene expression could robustly distinguish MS GM pathology (NAGM and GML) from healthy control GM, with MS diagnosis explaining 71% of variability in factor GM_F1 (Figure S10B). Factor GM_F1 explains equivalent variability in gene expression across glia (Figure S10B). Factor GM_F3 distinguishes GMLs from control, is predominantly neuronal (as GM_F2), and high factor GM_F3 is characterized by downregulation of genes related to OXPHOS, the electron transport chain, and protein folding (Data S1 and S6), indicating altered metabolism and mitochondrial function, as previously described in MS brain samples.^{33,34} To investigate whether neuronal compositional differences within the GM cortex influence the analysis, we reran the MOFA analysis without the neurons. This also identified five factors that correlated very strongly with the original GM MOFA factors, with the exception of the original GM_F3 factor (Data S1). No new factor had a strong correlation with original GM_F3, but as this factor is entirely determined by gene expression in neurons, this is expected (Data S1). Within each donor, factor values for all samples were very similar (Figure S10C), reflecting the gene expression similarities within one donor (Figure S10B).

MOFA WM factor scores (WM_F1-5) clearly distinguished MS patients from controls and also stratified MS patients into distinct subgroups (Figure 3A). Very similar factors were found using the orthogonal method Single-Cell Interpretable Tensor Decomposition (scITD)³⁵ (Data S1; STAR Methods). Four subgroups of MS patients had a distinct pattern of high/low factor scores across factors WM_F1-4, being either factor WM_F1, WM_F2, WM_F3, or WM_F4 high; scores for factor WM_F5 showed more variability across donors (Figure 3B). These apparent subgroups were not explained by lesion type (Figure 3A) or any available known metadata, including sex, type of MS, age, PMI, brain bank origin (Data S1), or differences in technical quality (Data S1). To infer potential mechanisms, we examined the genes driving these factors and found that, broadly, factors WM_F1-4 described glial responses to damage, while WM_F5 described an astrocyte regenerative response (Figure S10D). More specifically, high factor WM_F1 scores were characterized by a pan-glial upregulation of genes involved in protein folding, chaperone proteins, and ubiquitination (e.g., *HSPB1*, *HSPA4L*, *HSP90AA*, *BAG3*, *SERPINH1*, as found in other neurodegenerative diseases^{36,37}) and a reduced microglial expression of *CX3CR1*, *P2RY12*, and *P2RY13* (homeostatic markers), suggesting an adaptive cellular response to stress (Figure 3C; Data S1 and S6). High factor WM_F2 genes were characterized by cross-glial upregulation of genes in the integrated stress response, DNA damage, growth arrest, and apoptosis pathways, including *GADD45A*, *GADD45B*,³⁸ and *NAMPT* (Figure 3D). Factor WM_F3, which affects oligodendroglia most strongly, was characterized by the upregulation of extracellular matrix (ECM) genes, including *COL19A1*,

COL22A1, *TNC*, and *ITGB4* (Figure 3E), described to inhibit oligodendrocyte maturation and reduce myelination.^{39,40} High factor WM_F3 was also associated with the downregulation of *CRYAB* (alpha-crystallin B), which is thought to be protective in demyelination⁴¹ and is of interest due to its protein homology to Epstein-Barr virus nuclear antigen 1 with its association with MS diagnosis.⁴² Factor WM_F4 also affected oligodendroglia most strongly, but was characterized by the upregulation of major histocompatibility complex (MHC) class 1 molecules (*HLA-B* and *HLA-C*), previously described as upregulated in oligodendroglia in MS lesions and in preclinical mouse models of experimental autoimmune encephalomyelitis (EAE), targeting them for destruction,^{10,30} as well as the immune-related gene *ARHGAP24* described before as expressed in oligodendrocytes.⁴³ In addition, WM_F4 was associated with genes whose upregulation is associated with efforts to increase oligodendrogenesis, oligodendrocyte differentiation, and myelination (e.g., *SFRP1*⁴⁴ and *ANGPT2* similar to *ANGPTL2*⁴⁵; Figure 3F). Finally, factor WM_F5, affecting only astrocytes, was characterized by a strong upregulation of genes relating to primary cilia, including *DNAH11+6*, *SPAG17*, *ZBBX*, and *CFAP54* (Figure 3G). Ciliated astrocytes are thought to be pro-regenerative,⁴⁶ although may become longer and dysfunctional in disease.⁴⁷⁻⁴⁹

To further investigate whether these WM factors could describe different degenerative and regenerative pathological responses, we compared glial cellular compositional changes in samples and WM factor values (Figure 3H). High factors WM_F1-3 were associated with fewer oligodendrocyte types (Oligo_B-D), consistent with a general loss of oligodendrocytes and/or conversion to other more disease-related types. High factor WM_2 was associated with increases in Oligo_F and G (high in stress genes), reactive astrocytes (Astro_D-F), and reactive microglia (Micro_C), whereas high factor WM_F1 was associated with a marked reduction in the homeostatic microglia Micro_A, and to a lesser extent Micro_B and E. Oligo_G was increased in factors WM_1, 2, and 4. In addition, increased WM_F4 (affecting oligodendroglia most strongly) showed a reduction in Oligo_D, the subtype making most myelin transcripts, with no reduction in the immature subtypes. As WM_F4 is associated with genes related to increased oligodendrocyte differentiation and myelination, this may suggest that the regenerative response is mounted but blocked, and maturation fails. The increase in microglial subtypes Micro_A and B (with homeostatic markers) with increasing WM_F4 may also suggest an attempted regenerative response, since oligodendroglial crosstalk with specific microglial populations is essential in effective regeneration.^{50,51} High factor WM_F5 (affecting astrocytes most strongly) was markedly associated with ciliated astrocytes (astro-ciliated), with their proposed beneficial effect.⁴⁶ Thus, factor-based analysis correlated with differential cell type composition and allows us to propose stratification of the majority of MS donors by WM pathology phenotype: pattern 1 (stressed—chaperone response), pattern 2 (stressed—DNA damage), pattern 3 (inhibitory ECM response), pattern 4 (immune and blocked regenerative oligodendrocyte response) in combination with a more variable expression of a regenerative astrocyte response.

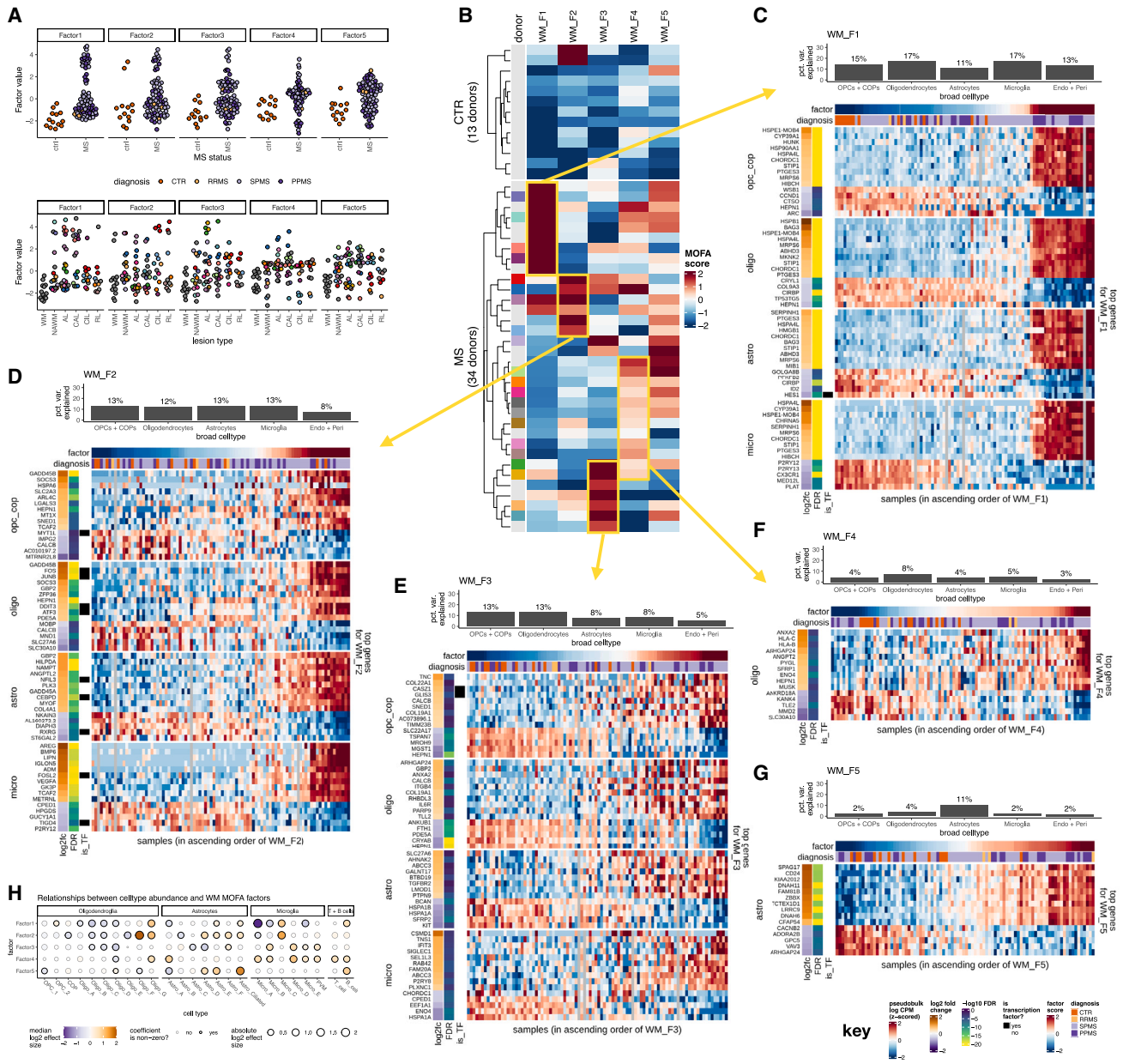


Figure 3. Patient stratification by WM factor values

(A) MOFA+ WM factor values (WM_F1–5) for control and MS samples, showing no correlation with WML type.

(B) Heat map of MOFA+ factors (columns) with signs changed to positively correlate with MS status, with donors in rows. Yellow boxes point to (C)–(G) showing genes driving each factor including a bar plot showing percentage (pct) variance explained by the factor in each broad cell type, and a heatmap of 15 genes with largest absolute factor weights for each cell type (10 increased, 5 decreased) where $\geq 10\%$ variance is explained by factor. Columns are samples, ordered in increasing order of factor score (top bar). Rows are genes, split by broad cell type. Heatmap colors are log CPM of pseudobulk expression, Z scored within each row; gray indicates insufficient cells of this cell type in the sample. Column annotations show log₂FC, FDR, and whether the gene is a transcription factor.

(C–G) (C) WM factor 1, (D) WM factor 2, (E) WM factor 3, (F) WM factor 4, and (G) WM factor 5. Key bottom right.

(H) Dot plot showing the relationship between cell type abundance of glial and immune cell subclusters and WM MOFA factors.

Validation of proposed patient stratification in other MS cohorts

To investigate whether the patient stratification identified by our MOFA+ approach was unique to our MS dataset (cohort I) or could also stratify other MS patients, we analyzed an indepen-

dent snRNA-seq cohort (cohort II) of 43 WM samples from 21 MS donors and 8 control donors (Figure 4A). Using the same workflow as before (see STAR Methods), after QC, we were able to include 10 new WM MS samples (referred to here as cohort IIa) and WM samples from published datasets (cohort

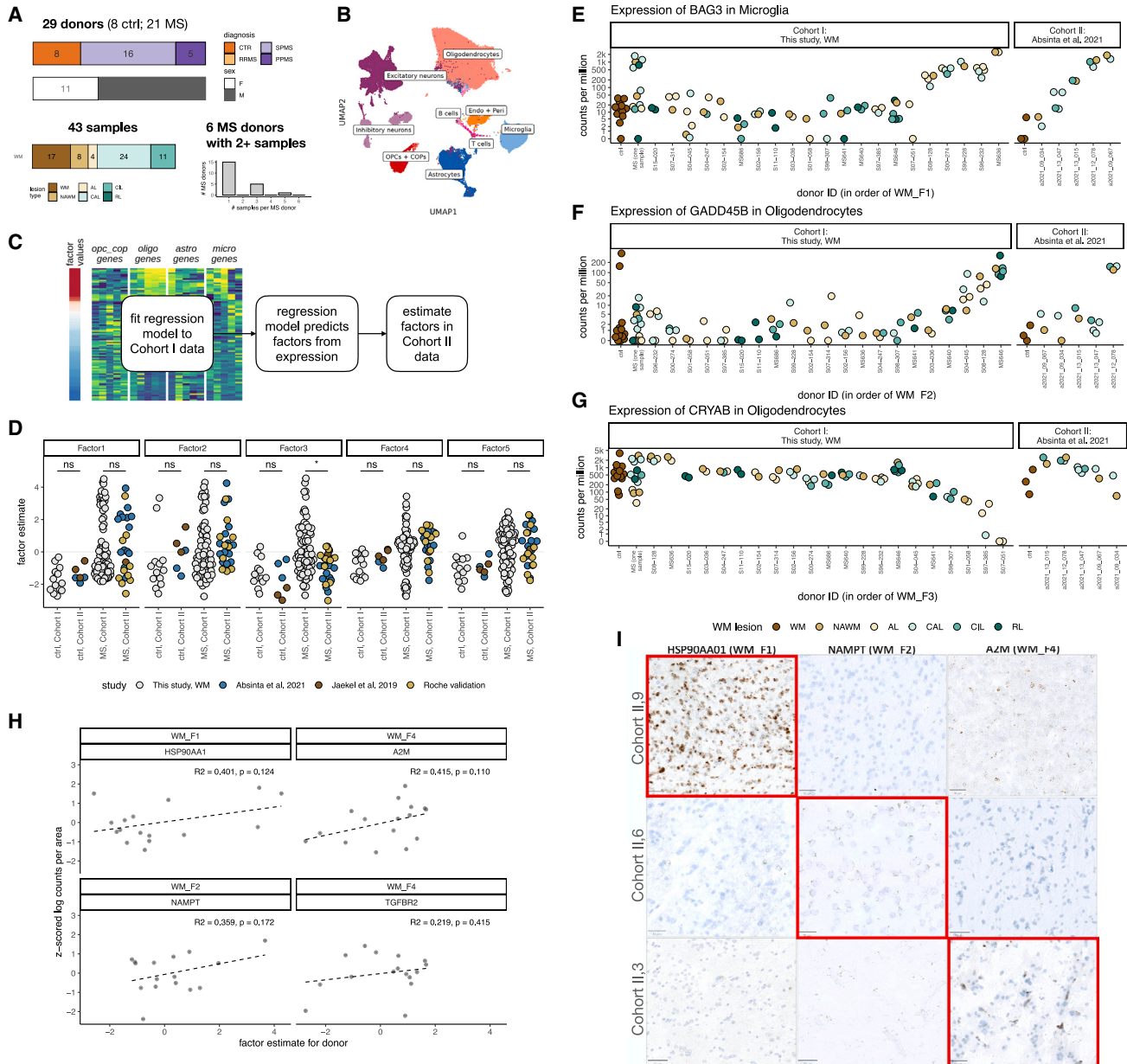


Figure 4. Second cohort dataset for validation

(A) Overview of cohort II donor and sample characteristics (CTR, control; RRMS, relapsing-remitting MS; SPMS, secondary progressive MS; PPMS, primary progressive MS)

(B) UMAP plot of cell types of cohorts I and II combined to show similarity. (Endo + Peri, endothelial cells and pericytes.)

(C) Cartoon of how the regression model is applied to data for factor estimates.

(D) Factor estimates for cohort II compared to cohort I factor values colored by dataset. Annotations show results of Kolmogorov-Smirnov test of whether the compared distributions are the same; p values adjusted with Benjamini-Hochberg method; n.s., not significant; *adjusted $p < 0.05$ and > 0.01 .

(E–G) Gene expression of selected genes related to WM factors in selected broad cell types, in controls, single samples per donor for datasets, and multiple samples per donor for cohort I and cohort II, ordered by WM factor level expression, (E) *BAG3* (WM_F1), (F) *GADD45B* (WM_F2), and (G) *CRYAB* (WM_F3).

(H) Graphs of Z score for RNAscope signal for four probes that showed positive correlation when plotted against factor value for each validation sample. R^2 and p values calculated with `cor.test` function in R, using method = "Pearson."

(I) Examples of RNAscope staining (see STAR Methods for details). Scale bar indicates 50 μ m.

IIb, including 14 MS samples and 3 controls from the Absinta et al. dataset⁹ and 1 MS donor and 3 controls from our previous Jäkel et al. dataset⁷). The Absinta et al. dataset⁹ contained 5 MS donors, each with 2–4 samples, whereas the rest were single samples from single donors. Datasets (e.g., Schirmer et al.⁸) containing mixed WM and GM samples could not be included.

The integration of the new cohort II with cohort I showed the same broad cell clusters (Figure 4B). We then implemented a regression model that allows us to estimate factor values acquired from a snRNA-seq cohort to any new snRNA-seq cohort dataset (which could be MS or any other neurological disease) (Figure 4C; STAR Methods). We used this regression model to estimate cohort I WM factor values in cohort II (Figure 4C) and found that the validation samples showed very similar distributions of WM factor values as in the discovery data, with the exception of WM-F3, which may relate to the low sample size (Figure 4D). In addition, visualization of examples of genes driving these factors (e.g., WM_F1: *BAG3*) across multiple samples of the cohort II dataset indicated similar expression across different lesion types and distinct expression across MS individuals, adding evidence to the global donor effect rather than lesion effect (Figures 4E–4G). Thus, these different MS pathological phenotypes were also identified in distinct subsets of patients in independent MS cohorts.

Furthermore, we performed validation of patient stratification based on WM_F1–4 using RNAscope in WM tissue blocks from 14 MS patients (5 donors from cohort I and 9 donors from cohort II) for whom we had WM_F1–F4 values derived or estimated from MOFA analyses of their snRNA-seq profiles as described above, with a range of values. Although the factor groupings are based on many hundreds of genes with different weightings, we selected three genes each for WM_F1–4, as these factors clearly grouped donors (see STAR Methods for RNAscope gene selection) with the hypothesis that RNAscope quantifications of WM_F1–F4 genes would show good correlation with their respective WM_F1–F4 values. Some of these genes did not present differences, possibly related to the low sample size. Notably, however, we found that *HSP90AA1* positively correlated with WM_F1, *NAMPT* with WM_F2, and *A2M* and *TGFBR* with WM_F4, but not with the chosen probes for WM_F3 (Figures 4H and 4I; further examples in Figures S11A and S11B). Overall, this proof-of-concept validation in a small sample size of MS patients corroborates the concept of patient stratification and indicates that factor markers can constitute biomarkers for distinct MS patient groups.

DISCUSSION

This snRNA-seq study on the most extensive cohort of MS patients to date provides an extensive resource for the community. It shows that GM and WM biology in MS are fundamentally different at a molecular and cellular level: while GM changes relate to the presence of a demyelinated lesion and patient ID, WM MS biology is more complex. Although there are cellular compositional and transcriptional differences present in each of the classical MS WML categories, as we would expect, the gene expression patterns of cells with different lesions are surprisingly mostly agnostic to the lesion environment and are

instead associated more with individual patient effects. These global patient effects allow us to take the first step toward the stratification of progressive MS patients by their molecular and cellular pathology, only made possible by the large number of samples captured both within individuals and from different individuals. Recent work has explored the trade-offs between read depth and number of individuals,⁵² finding greater read depth is useful for characterizing lowly expressed genes and rare cell types, but our study suggests that there is also much to be discovered by increasing the breadth of patient samples.

Our WM results point to four fundamentally different neurodegenerative pathological phenotypes in MS, selective for a subgroup of patients and shared by all WMLs and NAWM in a single patient: first, where there is a cross-gial stress response with increased protein folding/chaperone/ubiquitination pathways (pattern 1 stressed—chaperone response). Second, where there is an alternative cross-gial DNA damage stress response (pattern 2 stressed—DNA damage). Third, where there is an increased inhibitory ECM response to oligodendroglial differentiation (pattern 3—inhibitory ECM response). Fourth, where there is an immune oligodendrocyte response and a failure in the final stage of oligodendrocyte maturation (pattern 4—immune response). Superimposed on these is an apparent regenerative astrocyte response. None of these phenotypes group with any available patient metadata including age, sex, type of progressive MS, previous medications, post-mortem delay, sample quality measures, or disease duration, with the lack of association with the latter suggesting that phenotype does not change over the course of the disease (Data S1; Figure S10E). The proposal that distinct pathological processes underpin heterogeneity between MS patients is reminiscent of the previous work of Lucchinetti et al., who divided different patient pathological responses into patterns I–IV on the basis of lesion composition, analyzing numbers of oligodendrocytes, T cells, and microglia, as well as amount of immunoglobulins, complement, and myelin protein by immunohistochemistry.⁵³ On this basis, even without the benefit of current high-resolution techniques, all lesion samples from a given MS donor were of the same pathological pattern. Comparison of our WM factor values with the composition of our samples (nearest to the Lucchinetti classification) (Figure 3H) shows some possible overlap. Donors high in WM_F1 or WM_F2 have fewer oligodendrocytes and more stressed/diseased oligodendrocytes and may correspond to Lucchinetti pattern III, while donors high in WM_F4 or WM_F5 have increased numbers of B cells (making immunoglobulins) and may correspond to Lucchinetti type II (with increased plasma cells).

A key prediction of our results is that each patient group expressing one of WM factors 1–4 will respond best to different neuroprotective/regenerative therapies. This may help explain the apparent poor response to neuroprotective/pro-regenerative therapies in progressive MS trials—beneficial effects may have been missed due to the inability to perform appropriate (factor-based) subgroup analysis. Any positive response in these trials may be “diluted” by patient heterogeneity, and effective therapies for one subgroup may be lost. We propose that pro-remyelinating drugs acting through increasing oligodendrocyte maturation may be most effective in the patient subgroup patterns 3

and 4, where oligodendrocytes stall in differentiation, and not in those subgroups where the need is to reduce cellular stress. It is also conceivable that siponimod, now approved for selected SPMS patients, may have a more marked effect in the pattern 2 (stressed—DNA damage) subgroup, through its proposed role in NRF2 signaling and antioxidant pathways.⁵⁴

Our hypothesis that this MS patient stratification by pathology will convert into a clinically useful tool is yet to be proven. A blood-based stratification of relapsing-remitting MS patients into endophenotypes has recently been shown to correlate with efficacy upon interferon-beta treatment.⁵⁵ An effective patient stratification predicting brain pathological responses would give future clinical trials of neuroprotective agents the greatest power to reveal effective therapies. Our next step is to link these post-mortem phenotypes to biomarkers measurable in living individual, ideally in serum or cerebrospinal fluid (CSF), or perhaps even as targets for positron emission tomography (PET) ligands. We propose some initial possible biomarker candidates based on our initial validation studies. Encouragingly, consistent with our GM transcriptional change findings, it has already been shown that high protein levels of CSF parvalbumin correlated with the loss of PVALB+ inhibitory cortical neurons and increased MS disease severity.²⁴ Biomarker identification will allow us to determine whether pathological phenotypes are stable in the same patients over time⁵⁶ and to interrogate clinical trial datasets for effect or indeed lack of effect within post hoc stratified patient groups. Pathological subgroups may relate to genetic SNP variation, and SNPs are now emerging that relate to MS disease progression.⁵⁷ However, although we now have a large resource, we still currently lack the donor numbers required for these analyses. In the context of other neurodegenerative diseases, it will be interesting to determine whether any of these pathological patterns in response to MS are similar in subgroups of patients in response to Alzheimer's disease, Parkinson's disease, etc., or whether these are MS-specific. For example, multiple recent studies of Alzheimer's disease have discussed a microglia cluster similar to our Micro_D, characterized by high expression of *GPNMB* and other DAM signature genes.^{58,59}

In this study, we provide a resource of cell type-specific genes, whose expression distinguishes WM/GM pathology and subgroup phenotypes, to aid such future biomarker efforts. This is an essential step change for designing effective precision medicine therapeutic strategies for progressive MS—a critical unmet need.

Limitations of the study

A peripheral readout for CNS pathology in MS would be optimal in clinical settings for monitoring of the degenerative phase of the disease with stratification for prognosis and therapies. Our dataset, the largest snRNA-seq of MS samples yet, including WM and GM, and including multiple samples from the same donors, constitutes the first important step in this direction, providing a molecular blueprint of MS neuropathological responses. We anticipate that in the near future, with additional large MS cohorts where snRNA-seq CNS profiles can be integrated with blood/CSF datasets, and potentially SNP data, this will become possible.

For practical reasons, our study uses snRNA-seq from post-mortem archival tissues, with the limitation that this only evaluates primarily pre-mRNA nuclear transcripts. We undersampled rare immune cell populations, e.g., activated CD8 T cells, monocytes, dendritic cells, B cells, and MIMS,⁹ which are mostly enriched at the edges of chronically inflamed WMLs, perhaps as we focused on the entire lesion, but the sharing of gene expression programs across all lesions in oligodendrocytes, astrocytes, and microglia suggests the generalizability of our results. In addition, we cannot comment on subpial GMLs adjacent to compartmentalized inflammatory meningeal infiltrates,⁶⁰ as these were not in our dataset. We tried to match our MS donors and controls as well as possible, but differences (in banks, PMI, etc.) remain and differences will exist that we are unaware of. However, no results associated with any available patient metadata. Efforts to process clinical summaries from archival tissue from neurological patients with neurological disorders are now on the way.⁶¹ The integration of such studies with datasets as ours will be required in the future to link snRNA-seq based stratification with clinical criteria. Although we use a larger cohort of individuals than often used in single cell-omic studies, with all available and suitable public data for validation, even larger numbers will be required to validate our findings of patient groupings based on factor analysis at a transcriptional level, especially the high in factor WM-F3 group. Increasing the scope of our analysis with other modalities, for instance at the proteomics, lipidomics, and epigenomics level in future studies will help in the further characterization and stratification of MS patients.

RESOURCE AVAILABILITY

Lead contact

Further information and requests for data and other resources should be directed to and will be fulfilled by the lead contact, Anna Williams (anna.williams@ed.ac.uk).

Materials availability

This study did not generate new unique reagents.

Data and code availability

- All raw snRNA-seq data (FASTQ files) have been deposited to European Genome-Phenome Archive (EGA),⁶² as dataset EGA: EGAD00001009169.
- The cleaned annotated counts matrices, sample metadata, and cell type annotations for both cohorts are available on Zenodo: <https://doi.org/10.5281/zenodo.8338963>.
- R code and R markdown scripts used to do the analysis in the paper have been deposited at Zenodo: <https://doi.org/10.5281/zenodo.8338963>.
- An interactive web browser to analyze cell type-specific expression levels of genes and transcriptomic changes in MS versus control tissue is available at https://malhotralab.shinyapps.io/MS_broad/ (for broad cell types) and at https://malhotralab.shinyapps.io/MS_fine/ (for fine cell types).
- Any additional information required to reanalyze the data reported in this paper is available from the [lead contact](#) upon request.

ACKNOWLEDGMENTS

We thank Catharine Fournier Aquino and her team at the Functional Genomics Centre Zurich (FGCZ) for help with Illumina sequencing of 10× snRNA-seq

sample libraries; Kelly Bales and Irene Knuesel for their support with initiating this project; Pierre-Luc Germain at the University of Zurich, Switzerland, for assistance with gene module and *scDbtFinder* analysis; and members of Malhotra lab and Collin lab at Roche for fruitful discussions of the results. For the purpose of open access, the authors have applied a Creative Commons Attribution (CC BY) license to any Author Accepted Manuscript version arising from this submission. A.W. is funded by the MS Society UK, MRC, and the UKDRI (which is funded by the MRC, Alzheimer's Society, and Alzheimer's Research UK). G.C.-B. is funded by the Swedish Research Council (2019-01360), the European Union (2020 Research and Innovation Program/European Research Council Consolidator Grant EPISCOPE, 681893), Swedish Brain Foundation (FO2017-0075; FO2018-0162), Ming Wai Lau Centre for Reparative Medicine, Knut and Alice Wallenberg Foundation (grants 2019-0107; 2019-0089), Swedish Society for Medical Research (SSMF, grant JUB2019), the Göran Gustafsson Foundation for Research in Natural Sciences and Medicine, and Karolinska Institutet. E.A. was funded by the European Union, Horizon 2020, Marie-Sklodowska Curie Actions, grant SOLO, number 794689. F.A. was supported by the European Committee for Treatment and Research in Multiple Sclerosis (ECTRIMS). Resources were funded by F. Hoffmann-La Roche Ltd.

AUTHOR CONTRIBUTIONS

Conceptualization, D.M., A.W., G.C.-B., and C.f.-C.; data curation, W.M. and J.B.; formal analysis, W.M., J.B., P.K., S.J., E.A., E.H., M.D.R., and F.A.; investigation, D.C., S.J., A.W., S.A., M.M., E.N., N.S.-R., V.O., and R.M.; methodology, D.C., S.J., W.M., M.D.R., and R.S.S.; funding acquisition, D.M., A.W., and G.C.-B.; project administration, L.C.F., L.C., S.S., and E.U.; supervision, A.W., G.C.-B., D.M., and C.f.-C.; validation, W.M., D.C., R.S.S., and A.W.; visualization, W.M., R.S.S., and J.B.; writing – original draft, A.W., W.M., C.f.-C., G.C.-B., and D.M.; writing – review and editing, A.W., W.M., C.f.-C., G.C.-B., D.M., R.M., M.D.R., S.J., R.S.S., P.K., J.B., E.A., and D.C.

DECLARATION OF INTERESTS

The study was funded by F. Hoffmann-La Roche Ltd. D.C., J.B., W.M., L.C.F., L.C., E.U., and S.S. are full-time employees of F. Hoffmann-La Roche Ltd. D.M. was a full-time employee of F. Hoffmann-La Roche Ltd. and now works for Biogen.

STAR★METHODS

Detailed methods are provided in the online version of this paper and include the following:

- **KEY RESOURCES TABLE**
- **EXPERIMENTAL MODEL AND STUDY PARTICIPANT DETAILS**
 - Human tissue
- **METHOD DETAILS**
 - Sample preparation and single nuclei RNA sequencing
 - Immunohistochemistry and analysis
 - In Situ Hybridization on brain tissue - RNAscope
- **QUANTIFICATION AND STATISTICAL ANALYSIS**
 - Sample swap checks via genotyping
 - snRNAseq data processing and quality control
 - Data integration and clustering
 - Marker gene identification and cell type annotation
 - Differential abundance of cell types in MS lesions and control samples - *ANCOM-BC*
 - Differential abundance of cell types in MS lesions and control samples - *milor*
 - Differential expression analysis using generalised linear mixed models
 - Gene set enrichment analysis of differentially expressed genes
 - Assessment of cluster connectivity with *PAGA*
 - Patient stratification using *MOFA+*
 - Validation of *MOFA+* factors with *scITD*
 - Projection of *MOFA+* factors onto new cohort

- Selection of probes for validation of *MOFA+* factors by in situ hybridisation on tissue
- Contribution of model elements to cell type abundance variability
- Differential abundance of cell types in MS lesions and control samples
- Differential expression analysis using generalised linear mixed models
- Statistical analysis
- **ADDITIONAL RESOURCES**

SUPPLEMENTAL INFORMATION

Supplemental information can be found online at <https://doi.org/10.1016/j.neuron.2024.11.016>.

Received: November 16, 2023

Revised: September 11, 2024

Accepted: November 25, 2024

Published: December 20, 2024

REFERENCES

1. Lubetzki, C., Zalc, B., Williams, A., Stadelmann, C., and Stankoff, B. (2020). Remyelination in multiple sclerosis: from basic science to clinical translation. *Lancet Neurol.* *19*, 678–688. [https://doi.org/10.1016/S1474-4422\(20\)30140-X](https://doi.org/10.1016/S1474-4422(20)30140-X).
2. Chataway, J., De Angelis, F., Connick, P., Parker, R.A., Plantone, D., Doshi, A., John, N., Stutters, J., MacManus, D., Prados Carrasco, F., et al. (2020). Efficacy of three neuroprotective drugs in secondary progressive multiple sclerosis (MS-SMART): a phase 2b, multiarm, double-blind, randomised placebo-controlled trial. *Lancet Neurol.* *19*, 214–225. [https://doi.org/10.1016/S1474-4422\(19\)30485-5](https://doi.org/10.1016/S1474-4422(19)30485-5).
3. Cadavid, D., Mellion, M., Hupperts, R., Edwards, K.R., Calabresi, P.A., Drulović, J., Giovannoni, G., Hartung, H.-P., Arnold, D.L., Fisher, E., et al. (2019). Safety and efficacy of opicinumab in patients with relapsing multiple sclerosis (SYNERGY): a randomised, placebo-controlled, phase 2 trial. *Lancet Neurol.* *18*, 845–856. [https://doi.org/10.1016/S1474-4422\(19\)30137-1](https://doi.org/10.1016/S1474-4422(19)30137-1).
4. Brown, J.W.L., Cunniffe, N.G., Prados, F., Kanber, B., Jones, J.L., Needham, E., Georgieva, Z., Rog, D., Pearson, O.R., Overell, J., et al. (2021). Safety and efficacy of bexarotene in patients with relapsing-remitting multiple sclerosis (CCMR One): a randomised, double-blind, placebo-controlled, parallel-group, phase 2a study. *Lancet Neurol.* *20*, 709–720. [https://doi.org/10.1016/S1474-4422\(21\)00179-4](https://doi.org/10.1016/S1474-4422(21)00179-4).
5. Brown, J.W.L., Prados, F., Altmann, D.R., Kanber, B., Stutters, J., Cunniffe, N.G., Jones, J.L., Georgieva, Z.G., Needham, E.J., Darwalla, C., et al. (2022). Remyelination varies between and within lesions in multiple sclerosis following bexarotene. *Ann. Clin. Transl. Neurol.* *9*, 1626–1642. <https://doi.org/10.1002/acn3.51662>.
6. Green, A.J., Gelfand, J.M., Cree, B.A., Bevan, C., Boscardin, W.J., Mei, F., Inman, J., Arnow, S., Devereux, M., Abounasr, A., et al. (2017). Clemastine fumarate as a remyelinating therapy for multiple sclerosis (ReBUILD): a randomised, controlled, double-blind, crossover trial. *Lancet* *390*, 2481–2489. [https://doi.org/10.1016/S0140-6736\(17\)32346-2](https://doi.org/10.1016/S0140-6736(17)32346-2).
7. Jäkel, S., Agirre, E., Mendanha Falcão, A., van Bruggen, D., Lee, K.W., Knuesel, I., Malhotra, D., Ffrench-Constant, C., Williams, A., and Castelo-Branco, G. (2019). Altered human oligodendrocyte heterogeneity in multiple sclerosis. *Nature* *566*, 543–547. <https://doi.org/10.1038/s41586-019-0903-2>.
8. Schirmer, L., Velmeshev, D., Holmqvist, S., Kaufmann, M., Werneburg, S., Jung, D., Vistnes, S., Stockley, J.H., Young, A., Steindel, M., et al. (2019). Neuronal vulnerability and multi-lineage diversity in multiple sclerosis. *Nature* *573*, 75–82. <https://doi.org/10.1038/s41586-019-1404-z>.
9. Absinta, M., Maric, D., Gharagozloo, M., Garton, T., Smith, M.D., Jin, J., Fitzgerald, K.C., Song, A., Liu, P., Lin, J.-P., et al. (2021). A

- lymphocyte-microglia-astrocyte axis in chronic active multiple sclerosis. *Nature* 597, 709–714. <https://doi.org/10.1038/s41586-021-03892-7>.
10. Falcão, A.M., van Bruggen, D., Marques, S., Meijer, M., Jäkel, S., Agirre, E., Samudiyata, F., Floriddia, E.M., Vanichkina, D.P., Ffrench-Constant, C., et al. (2018). Disease-specific oligodendrocyte lineage cells arise in multiple sclerosis. *Nat. Med.* 24, 1837–1844. <https://doi.org/10.1038/s41591-018-0236-y>.
 11. Hilscher, M.M., Langseth, C.M., Kukanja, P., Yokota, C., Nilsson, M., and Castelo-Branco, G. (2022). Spatial and temporal heterogeneity in the lineage progression of fine oligodendrocyte subtypes. *BMC Biol.* 20, 122. <https://doi.org/10.1186/s12915-022-01325-z>.
 12. Gelman, A. (2008). Scaling regression inputs by dividing by two standard deviations. *Stat. Med.* 27, 2865–2873. <https://doi.org/10.1002/sim.3107>.
 13. Fleming, S.J., Chaffin, M.D., Arduini, A., Akkad, A.-D., Banks, E., Marioni, J.C., Philippakis, A.A., Ellinor, P.T., and Babadi, M. (2023). Unsupervised removal of systematic background noise from droplet-based single-cell experiments using CellBender. *Nat. Methods* 20, 1323–1335. <https://doi.org/10.1038/s41592-023-01943-7>.
 14. Lassmann, H. (2018). Multiple sclerosis pathology. *Cold Spring Harb. Perspect. Med.* 8, a028936. <https://doi.org/10.1101/cshperspect.a028936>.
 15. Hao, Y., Hao, S., Andersen-Nissen, E., Mauck, W.M., 3rd, Zheng, S., Butler, A., Lee, M.J., Wilk, A.J., Darby, C., Zager, M., et al. (2021). Integrated analysis of multimodal single-cell data. *Cell* 184, 3573–3587.e29. <https://doi.org/10.1016/j.cell.2021.04.048>.
 16. Korsunsky, I., Millard, N., Fan, J., Slowikowski, K., Zhang, F., Wei, K., Baglaenko, Y., Brenner, M., Loh, P.-R., and Raychaudhuri, S. (2019). Fast, sensitive and accurate integration of single-cell data with Harmony. *Nat. Methods* 16, 1289–1296. <https://doi.org/10.1038/s41592-019-0619-0>.
 17. Barkas, N., Petukhov, V., Nikolaeva, D., Lozinsky, Y., Demharter, S., Khodosevich, K., and Kharchenko, P.V. (2019). Joint analysis of heterogeneous single-cell RNA-seq dataset collections. *Nat. Methods* 16, 695–698. <https://doi.org/10.1038/s41592-019-0466-z>.
 18. Seeker, L.A., Bestard-Cuche, N., Jäkel, S., Kazakou, N.-L., Bøstrand, S.M.K., Wagstaff, L.J., Cholewa-Waclaw, J., Kilpatrick, A.M., Van Bruggen, D., Kabbe, M., et al. (2023). Brain matters: unveiling the distinct contributions of region, age, and sex to glia diversity and CNS function. *Acta Neuropathol. Commun.* 11, 84. <https://doi.org/10.1186/s40478-023-01568-z>.
 19. Wolf, F.A., Hamey, F.K., Plass, M., Solana, J., Dahlin, J.S., Göttgens, B., Rajewsky, N., Simon, L., and Theis, F.J. (2019). PAGA: graph abstraction reconciles clustering with trajectory inference through a topology preserving map of single cells. *Genome Biol.* 20, 59. <https://doi.org/10.1186/s13059-019-1663-x>.
 20. Engel, T., Kannenberg, F., Fobker, M., Nofer, J.-R., Bode, G., Lueken, A., Assmann, G., and Seedorf, U. (2007). Expression of ATP binding cassette-transporter ABCG1 prevents cell death by transporting cytotoxic 7beta-hydroxycholesterol. *FEBS Lett.* 581, 1673–1680. <https://doi.org/10.1016/j.febslet.2007.03.038>.
 21. Pandey, S., Shen, K., Lee, S.-H., Shen, Y.-A.A., Wang, Y., Otero-García, M., Kotova, N., Vito, S.T., Laufer, B.I., Newton, D.F., et al. (2022). Disease-associated oligodendrocyte responses across neurodegenerative diseases. *Cell Rep.* 40, 111189. <https://doi.org/10.1016/j.celrep.2022.111189>.
 22. Batiuk, M.Y., Martirosyan, A., Wahis, J., de Vin, F., Marneffe, C., Kusserow, C., Koeppen, J., Viana, J.F., Oliveira, J.F., Voet, T., et al. (2020). Identification of region-specific astrocyte subtypes at single cell resolution. *Nat. Commun.* 11, 1220. <https://doi.org/10.1038/s41467-019-14198-8>.
 23. Paolicelli, R.C., Sierra, A., Stevens, B., Tremblay, M.-E., Aguzzi, A., Ajami, B., Amit, I., Audinat, E., Bechmann, I., Bennett, M., et al. (2022). Microglia states and nomenclature: A field at its crossroads. *Neuron* 110, 3458–3483. <https://doi.org/10.1016/j.neuron.2022.10.020>.
 24. Magliozzi, R., Pitteri, M., Ziccardi, S., Pisani, A.I., Montibeller, L., Marastoni, D., Rossi, S., Mazziotti, V., Guandalini, M., Dapor, C., et al. (2021). CSF parvalbumin levels reflect interneuron loss linked with cortical pathology in multiple sclerosis. *Ann. Clin. Transl. Neurol.* 8, 534–547. <https://doi.org/10.1002/acn3.51298>.
 25. Zoupi, L., Booker, S.A., Eigel, D., Werner, C., Kind, P.C., Spires-Jones, T.L., Newland, B., and Williams, A.C. (2021). Selective vulnerability of inhibitory networks in multiple sclerosis. *Acta Neuropathol.* 141, 415–429. <https://doi.org/10.1007/s00401-020-02258-z>.
 26. Albert, M., Antel, J., Brück, W., and Stadelmann, C. (2007). Extensive cortical remyelination in patients with chronic multiple sclerosis. *Brain Pathol.* 17, 129–138. <https://doi.org/10.1111/j.1750-3639.2006.00043.x>.
 27. Dann, E., Henderson, N.C., Teichmann, S.A., Morgan, M.D., and Marioni, J.C. (2022). Differential abundance testing on single-cell data using k-nearest neighbor graphs. *Nat. Biotechnol.* 40, 245–253. <https://doi.org/10.1038/s41587-021-01033-z>.
 28. Brooks, M., Kristensen, K., van Benthem, K., Magnusson, A., Berg, C., Nielsen, A., Skaug, H., Mächler, M., and Bolker, B. (2017). GlmmTMB balances speed and flexibility among packages for zero-inflated generalized linear mixed modeling. *R J.* 9, 378. <https://doi.org/10.32614/RJ-2017-066>.
 29. Van Doorn, R., Van Horsen, J., Verzijl, D., Witte, M., Ronken, E., Van Het Hof, B., Lakeman, K., Dijkstra, C.D., Van Der Valk, P., Reijerkerk, A., et al. (2010). Sphingosine 1-phosphate receptor 1 and 3 are upregulated in multiple sclerosis lesions: SIP Receptor 1 and 3 are Upregulated in MS Lesions. *Glia* 58, 1465–1476. <https://doi.org/10.1002/glia.21021>.
 30. Kirby, L., Jin, J., Cardona, J.G., Smith, M.D., Martin, K.A., Wang, J., Strasburger, H., Herbst, L., Alexis, M., Karnell, J., et al. (2019). Oligodendrocyte precursor cells present antigen and are cytotoxic targets in inflammatory demyelination. *Nat. Commun.* 10, 3887. <https://doi.org/10.1038/s41467-019-11638-3>.
 31. Argelaguet, R., Arnol, D., Bredikhin, D., Deloro, Y., Velten, B., Marioni, J.C., and Stegle, O. (2020). MOFA+: a statistical framework for comprehensive integration of multi-modal single-cell data. *Genome Biol.* 21, 111. <https://doi.org/10.1186/s13059-020-02015-1>.
 32. Ramirez Flores, R.O., Lanzer, J.D., Dimitrov, D., Velten, B., and Saez-Rodriguez, J. (2023). Multicellular factor analysis of single-cell data for a tissue-centric understanding of disease. *eLife* 12, e93161. <https://doi.org/10.7554/eLife.93161>.
 33. Mahad, D., Ziabreva, I., Lassmann, H., and Turnbull, D. (2008). Mitochondrial defects in acute multiple sclerosis lesions. *Brain* 131, 1722–1735. <https://doi.org/10.1093/brain/awn105>.
 34. Mahad, D.J., Ziabreva, I., Campbell, G., Lax, N., White, K., Hanson, P.S., Lassmann, H., and Turnbull, D.M. (2009). Mitochondrial changes within axons in multiple sclerosis. *Brain* 132, 1161–1174. <https://doi.org/10.1093/brain/awp046>.
 35. Mitchel, J., Gordon, M.G., Perez, R.K., Biederstedt, E., Bueno, R., Ye, C.J., and Kharchenko, P.V. (2024). Coordinated, multicellular patterns of transcriptional variation that stratify patient cohorts are revealed by tensor decomposition. *Nat. Biotechnol.* <https://doi.org/10.1038/s41587-024-02411-z>.
 36. Askenazi, M., Kavanagh, T., Pires, G., Ueberheide, B., Wisniewski, T., and Drummond, E. (2023). Compilation of reported protein changes in the brain in Alzheimer’s disease. *Nat. Commun.* 14, 4466. <https://doi.org/10.1038/s41467-023-40208-x>.
 37. Bøstrand, S.M.K., Seeker, L.A., Bestard-Cuche, N., Kazakou, N.-L., Jäkel, S., Kenkhuis, B., Henderson, N.C., de Bot, S.T., van Roon-Mom, W.M.C., Priller, J., et al. (2024). Mapping the glial transcriptome in Huntington’s disease using snRNAseq: selective disruption of glial signatures across brain regions. *Acta Neuropathol. Commun.* 12, 165. <https://doi.org/10.1186/s40478-024-01871-3>.

38. Humayun, A., and Fornace, A.J., Jr. (2022). GADD45 in stress signaling, cell cycle control, and apoptosis. *Adv. Exp. Med. Biol.* 1360, 1–22. https://doi.org/10.1007/978-3-030-94804-7_1.
39. Czopka, T., von Holst, A., French-Constant, C., and Faissner, A. (2010). Regulatory mechanisms that mediate tenascin C-dependent inhibition of oligodendrocyte precursor differentiation. *J. Neurosci.* 30, 12310–12322. <https://doi.org/10.1523/JNEUROSCI.4957-09.2010>.
40. Laursen, L.S., and French-Constant, C. (2007). Adhesion molecules in the regulation of CNS myelination. *Neuron Glia Biol.* 3, 367–375. <https://doi.org/10.1017/S1740925X08000161>.
41. Ousman, S.S., Tomooka, B.H., van Noort, J.M., Wawrousek, E.F., O'Connor, K.C., Hafler, D.A., Sobel, R.A., Robinson, W.H., and Steinman, L. (2007). Protective and therapeutic role for alphaB-crystallin in autoimmune demyelination. *Nature* 448, 474–479. <https://doi.org/10.1038/nature05935>.
42. Thomas, O.G., Bronge, M., Tengvall, K., Akpinar, B., Nilsson, O.B., Holmgren, E., Hessa, T., Gafvelin, G., Khademi, M., Alfredsson, L., et al. (2023). Cross-reactive EBNA1 immunity targets alpha-crystallin B and is associated with multiple sclerosis. *Sci. Adv.* 9, eadg3032. <https://doi.org/10.1126/sciadv.adg3032>.
43. Kokkosis, A.G., Madeira, M.M., Mullahy, M.R., and Tsrirka, S.E. (2022). Chronic stress disrupts the homeostasis and progeny progression of oligodendroglial lineage cells, associating immune oligodendrocytes with prefrontal cortex hypomyelination. *Mol. Psychiatry* 27, 2833–2848. <https://doi.org/10.1038/s41380-022-01512-y>.
44. Huang, S., Choi, M.H., Huang, H., Wang, X., Chang, Y.C., and Kim, J.Y. (2020). Demyelination regulates the circadian transcription factor BMAL1 to signal adult neural stem cells to initiate oligodendrogenesis. *Cell Rep.* 33, 108394. <https://doi.org/10.1016/j.celrep.2020.108394>.
45. Chen, L., Yu, Z., Xie, L., He, X., Mu, X., Chen, C., Yang, W., Tong, X., Liu, J., Gao, Z., et al. (2023). ANGPTL2 binds MAG to efficiently enhance oligodendrocyte differentiation. *Cell Biosci.* 13, 42. <https://doi.org/10.1186/s13578-023-00970-3>.
46. Ki, S.M., Jeong, H.S., and Lee, J.E. (2021). Primary cilia in glial cells: an oasis in the journey to overcoming neurodegenerative diseases. *Front. Neurosci.* 15, 736888. <https://doi.org/10.3389/fnins.2021.736888>.
47. Sterpka, A., Yang, J., Strobel, M., Zhou, Y., Pauplis, C., and Chen, X. (2020). Diverged morphology changes of astrocytic and neuronal primary cilia under reactive insults. *Mol. Brain* 13, 28. <https://doi.org/10.1186/s13041-020-00571-y>.
48. Ignatenko, O., Malinen, S., Rybas, S., Vihinen, H., Nikkanen, J., Kononov, A., Jokitalo, E.S., Ince-Dunn, G., and Suomalainen, A. (2023). Mitochondrial dysfunction compromises ciliary homeostasis in astrocytes. *J. Cell Biol.* 222, e202203019. <https://doi.org/10.1083/jcb.202203019>.
49. Lerma-Martin, C., Badia-i-Mompel, P., Flores, R.O.R., Sekol, P., Hofmann, A., Thawel, T., Riedl, C.J., Wuennemann, F., Ibarra-Arellano, M.A., Trobisch, T., et al. (2024). Cell type mapping reveals tissue niches and interactions in subcortical multiple sclerosis lesions. *Nat. Neurosci.* 27, 2354–2365. <https://doi.org/10.1038/s41593-024-01796-z>.
50. Miron, V.E., Boyd, A., Zhao, J.-W., Yuen, T.J., Ruckh, J.M., Shadrach, J.L., van Wijngaarden, P., Wagers, A.J., Williams, A., Franklin, R.J.M., et al. (2013). M2 microglia and macrophages drive oligodendrocyte differentiation during CNS remyelination. *Nat. Neurosci.* 16, 1211–1218. <https://doi.org/10.1038/nn.3469>.
51. Dillenburger, A., Ireland, G., Holloway, R.K., Davies, C.L., Evans, F.L., Swire, M., Bechler, M.E., Soong, D., Yuen, T.J., Su, G.H., et al. (2018). Activin receptors regulate the oligodendrocyte lineage in health and disease. *Acta Neuropathol.* 135, 887–906. <https://doi.org/10.1007/s00401-018-1813-3>.
52. Schmid, K.T., Höllbacher, B., Cruceanu, C., Böttcher, A., Lickert, H., Binder, E.B., Theis, F.J., and Heinig, M. (2021). scPower accelerates and optimizes the design of multi-sample single cell transcriptomic studies. *Nat. Commun.* 12, 6625. <https://doi.org/10.1038/s41467-021-26779-7>.
53. Lucchinetti, C., Brück, W., Parisi, J., Scheithauer, B., Rodriguez, M., and Lassmann, H. (2000). Heterogeneity of multiple sclerosis lesions: implications for the pathogenesis of demyelination. *Ann. Neurol.* 47, 707–717. [https://doi.org/10.1002/1531-8249\(200006\)47:6<707::aid-ana3>3.0.co;2-q](https://doi.org/10.1002/1531-8249(200006)47:6<707::aid-ana3>3.0.co;2-q).
54. Colombo, E., Bassani, C., De Angelis, A., Ruffini, F., Ottoboni, L., Comi, G., Martino, G., and Farina, C. (2020). Siponimod (BAF312) activates Nrf2 while hampering NF κ B in human astrocytes, and protects from astrocyte-induced neurodegeneration. *Front. Immunol.* 11, 635. <https://doi.org/10.3389/fimmu.2020.00635>.
55. Gross, C.C., Schulte-Mecklenbeck, A., Steinberg, O.V., Wirth, T., Lauks, S., Bittner, S., Schindler, P., Baranzini, S.E., Groppa, S., Bellmann-Strobl, J., et al. (2024). Multiple sclerosis endophenotypes identified by high-dimensional blood signatures are associated with distinct disease trajectories. *Sci. Transl. Med.* 16, eade8560. <https://doi.org/10.1126/scitranslmed.ade8560>.
56. Metz, I., Gavriloiva, R.H., Weigand, S.D., Frischer, J.M., Popescu, B.F., Guo, Y., Gloth, M., Tobin, W.O., Zalewski, N.L., Lassmann, H., et al. (2021). Magnetic resonance imaging correlates of multiple sclerosis immunopathological patterns. *Ann. Neurol.* 90, 440–454. <https://doi.org/10.1002/ana.26163>.
57. International; Multiple; Sclerosis; Genetics Consortium; MultipleMS Consortium (2023). Locus for severity implicates CNS resilience in progression of multiple sclerosis. *Nature* 619, 323–331. <https://doi.org/10.1038/s41586-023-06250-x>.
58. Gazestani, V., Kamath, T., Nadaf, N.M., Dougalis, A., Burris, S.J., Rooney, B., Junkkari, A., Vanderburg, C., Pelkonen, A., Gomez-Budia, M., et al. (2023). Early Alzheimer's disease pathology in human cortex involves transient cell states. *Cell* 186, 4438–4453.e23. <https://doi.org/10.1016/j.cell.2023.08.005>.
59. Green, G.S., Fujita, M., Yang, H.-S., Taga, M., Cain, A., McCabe, C., Comandante-Lou, N., White, C.C., Schmidner, A.K., Zeng, L., et al. (2024). Cellular communities reveal trajectories of brain ageing and Alzheimer's disease. *Nature* 633, 634–645. <https://doi.org/10.1038/s41586-024-07871-6>.
60. Magliozzi, R., Howell, O.W., Durrenberger, P., Aricò, E., James, R., Cruciani, C., Reeves, C., Roncaroli, F., Nicholas, R., and Reynolds, R. (2019). Meningeal inflammation changes the balance of TNF signalling in cortical grey matter in multiple sclerosis. *J. Neuroinflammation* 16, 259. <https://doi.org/10.1186/s12974-019-1650-x>.
61. Mekkes, N.J., Groot, M., Hoekstra, E., de Boer, A., Dagkesamanskaia, E., Bouwman, S., Wehrens, S.M.T., Herbert, M.K., Wever, D.D., Rozemuller, A., et al. (2024). Identification of clinical disease trajectories in neurodegenerative disorders with natural language processing. *Nat. Med.* 30, 1143–1153. <https://doi.org/10.1038/s41591-024-02843-9>.
62. Lappalainen, I., Almeida-King, J., Kumanduri, V., Senf, A., Spalding, J.D., Ur-Rehman, S., Saunders, G., Kandasamy, J., Caccamo, M., Leinonen, R., et al. (2015). The European Genome-phenome Archive of human data consented for biomedical research. *Nat. Genet.* 47, 692–695. <https://doi.org/10.1038/ng.3312>.
63. Germain, P.-L., Lun, A., Macnair, W., and Robinson, M.D. (2021). Doublet identification in single-cell sequencing data using scDblFinder. *F1000Res* 10, 979. <https://doi.org/10.12688/f1000research.73600.1>.
64. Macnair, W., and Robinson, M. (2023). SampleQC: robust multivariate, multi-cell type, multi-sample quality control for single-cell data. *Genome Biol.* 24, 23.
65. Robinson, M.D., McCarthy, D.J., and Smyth, G.K. (2010). edgeR: a Bioconductor package for differential expression analysis of digital gene expression data. *Bioinformatics* 26, 139–140. <https://doi.org/10.1093/bioinformatics/btp616>.
66. Lin, H., and Peddada, S.D. (2020). Analysis of compositions of microbiomes with bias correction. *Nat. Commun.* 11, 3514. <https://doi.org/10.1038/s41467-020-17041-7>.

67. Korotkevich, G., Sukhov, V., and Sergushichev, A. (2019). Fast Gene Set Enrichment Analysis (Cold Spring Harbor Laboratory), p. 060012. <https://doi.org/10.1101/060012>.
68. Friedman, J., Hastie, T., and Tibshirani, R. (2010). Regularization paths for generalized linear models via coordinate descent. *J. Stat. Softw.* **33**, 1–22.
69. Trapp, B.D., Bö, L., Mörk, S., and Chang, A. (1999). Pathogenesis of tissue injury in MS lesions. *J. Neuroimmunol.* **98**, 49–56. [https://doi.org/10.1016/s0165-5728\(99\)00081-8](https://doi.org/10.1016/s0165-5728(99)00081-8).
70. Piddlesden, S.J., Lassmann, H., Zimprich, F., Morgan, B.P., and Lington, C. (1991). The demyelinating potential of antibodies to myelin oligodendrocyte glycoprotein is related to their ability to fix complement. *J. Neuroimmunol.* **35**, 111. [https://doi.org/10.1016/0165-5728\(91\)91046-F](https://doi.org/10.1016/0165-5728(91)91046-F).
71. Bankhead, P., Loughrey, M.B., Fernández, J.A., Dombrowski, Y., McArt, D.G., Dunne, P.D., McQuaid, S., Gray, R.T., Murray, L.J., Coleman, H.G., et al. (2017). QuPath: open source software for digital pathology image analysis. *Sci. Rep.* **7**, 16878. <https://doi.org/10.1038/s41598-017-17204-5>.
72. Schindelin, J., Arganda-Carreras, I., Frise, E., Kaynig, V., Longair, M., Pietzsch, T., Preibisch, S., Rueden, C., Saalfeld, S., Schmid, B., et al. (2012). Fiji: an open-source platform for biological-image analysis. *Nat. Methods* **9**, 676–682. <https://doi.org/10.1038/nmeth.2019>.
73. McCarthy, S., Das, S., Kretzschmar, W., Delaneau, O., Wood, A.R., Teumer, A., Kang, H.M., Fuchsberger, C., Danecek, P., Sharp, K., et al. (2016). A reference panel of 64,976 haplotypes for genotype imputation. *Nat. Genet.* **48**, 1279–1283. <https://doi.org/10.1038/ng.3643>.
74. Purcell, S., Neale, B., Todd-Brown, K., Thomas, L., Ferreira, M.A.R., Bender, D., Maller, J., Sklar, P., de Bakker, P.I.W., Daly, M.J., et al. (2007). PLINK: a tool set for whole-genome association and population-based linkage analyses. *Am. J. Hum. Genet.* **81**, 559–575. <https://doi.org/10.1086/519795>.
75. Fort, A., Panousis, N.I., Garieri, M., Antonarakis, S.E., Lappalainen, T., Dermizakis, E.T., and Delaneau, O. (2017). MBV: a method to solve sample mislabeling and detect technical bias in large combined genotype and sequencing assay datasets. *Bioinformatics* **33**, 1895–1897. <https://doi.org/10.1093/bioinformatics/btx074>.
76. Chen, T., and Guestrin, C. (2016). XGBoost: A scalable tree boosting system. Preprint at arXiv. <https://doi.org/10.1145/2939672.2939785>.
77. Hesterberg, T. (2011). Bootstrap. *WIREs Computational Stats.* **3**, 497–526. <https://doi.org/10.1002/wics.182>.
78. McCarthy, D.J., and Smyth, G.K. (2009). Testing significance relative to a fold-change threshold is a TREAT. *Bioinformatics* **25**, 765–771. <https://doi.org/10.1093/bioinformatics/btp053>.
79. Crowell, H.L., Soneson, C., Germain, P.-L., Calini, D., Collin, L., Raposo, C., Malhotra, D., and Robinson, M.D. (2020). muscat detects subpopulation-specific state transitions from multi-sample multi-condition single-cell transcriptomics data. *Nat. Commun.* **11**, 6077. <https://doi.org/10.1038/s41467-020-19894-4>.
80. Squair, J.W., Gautier, M., Kathe, C., Anderson, M.A., James, N.D., Hutson, T.H., Hudelle, R., Qaiser, T., Matson, K.J.E., Barraud, Q., et al. (2021). Confronting false discoveries in single-cell differential expression. *Nat. Commun.* **12**, 5692. <https://doi.org/10.1101/2021.03.12.435024>.
81. Liberzon, A., Subramanian, A., Pinchback, R., Thorvaldsdóttir, H., Tamayo, P., and Mesirov, J.P. (2011). Molecular signatures database (MSigDB) 3.0. *Bioinformatics* **27**, 1739–1740. <https://doi.org/10.1093/bioinformatics/btr260>.
82. Wickham, H. (2009). ggplot2: Elegant Graphics for Data Analysis (Springer). <https://doi.org/10.1007/978-0-387-98141-3>.
83. Wolf, F.A., Angerer, P., and Theis, F.J. (2018). SCANPY: large-scale single-cell gene expression data analysis. *Genome Biol.* **19**, 15. <https://doi.org/10.1186/s13059-017-1382-0>.
84. Love, M.I., Huber, W., and Anders, S. (2014). Moderated estimation of fold change and dispersion for RNA-seq data with DESeq2. *Genome Biol.* **15**, 550. <https://doi.org/10.1186/s13059-014-0550-8>.
85. Uhlén, M., Fagerberg, L., Hallström, B.M., Lindskog, C., Oksvold, P., Mardinoglu, A., Sivertsson, Å., Kampf, C., Sjöstedt, E., Asplund, A., et al. (2015). Proteomics. Tissue-based map of the human proteome. *Science* **347**, 1260419. <https://doi.org/10.1126/science.1260419>.
86. Uhlén, M., Karlsson, M.J., Hober, A., Svensson, A.-S., Scheffel, J., Kotol, D., Zhong, W., Tebani, A., Strandberg, L., Edfors, F., et al. (2019). The human secretome. *Sci. Signal.* **12**, eaaz0274. <https://doi.org/10.1126/scisignal.aaz0274>.
87. Wallen, Z.D. (2021). Comparison study of differential abundance testing methods using two large Parkinson disease gut microbiome datasets derived from 16S amplicon sequencing. *BMC Bioinformatics* **22**, 265. <https://doi.org/10.1186/s12859-021-04193-6>.
88. Buettner, M., Ostner, J., Mueller, C.L., Theis, F.J., and Schubert, B. (2020). scCODA: A Bayesian Model for Compositional Single-Cell Data Analysis (Cold Spring Harbor Laboratory). <https://doi.org/10.1101/2020.12.14.422688>.
89. Zimmerman, K.D., Espeland, M.A., and Langefeld, C.D. (2021). A practical solution to pseudoreplication bias in single-cell studies. *Nat. Commun.* **12**, 738. <https://doi.org/10.1038/s41467-021-21038-1>.
90. Hoffman, G.E., and Roussos, P. (2021). Dream: powerful differential expression analysis for repeated measures designs. *Bioinformatics* **37**, 192–201. <https://doi.org/10.1093/bioinformatics/btaa687>.
91. R Core Team (2013). R: A Language and Environment for Statistical Computing (R Foundation for Statistical Computing).

STAR★METHODS

KEY RESOURCES TABLE

REAGENT or RESOURCE	SOURCE	IDENTIFIER
Antibodies		
mouse anti-CNP	Atlas	RRID:AB_2665789
rabbit anti-human GPR17	Cayman Chemical	RRID:AB_10613826
Rat anti MBP aa82-87	BioRad	RRID:AB_10886666
Mouse anti-Myelin Proteolipid Protein Antibody	Millipore	RRID:AB_177623
MHCII	Dako	RRID:AB_2313661
rabbit-HRP IgG	Vector laboratories	RRID:AB_2336529
mouse-HRP IgG	Vector laboratories	RRID:AB_2336528
Deposited data		
snRNAseq data - new from this paper	Human brain, this paper	EGAD00001009169
snRNAseq data from Absinta et al.	Absinta et al. ⁹	EGA GSE180759
snRNAseq data from Jäkel et al.	Jäkel et al. ⁷	EGAS00001003412
snRNAseq data from Schirmer et al.	Schirmer et al. ⁸	Sequence Read Archive (SRA), accession number PRJNA544731 (NCBI Bioproject ID: 544731)
Software and algorithms		
Cleaned annotated counts matrices, sample metadata and cell type annotations for both cohorts, and R and R markdown scripts	This paper	https://doi.org/10.5281/zenodo.8338963
source code used to analyse the snRNA-seq data in the current study is available online at	This paper	https://zenodo.org/record/8338963
Cell Ranger	10x genomics	v3.1.0
CellBender	Fleming et al. ¹³	v0.2.2
velocity	https://velocity.org/	v0.17.17
scDbfFinder	Germain et al. ⁶³	v1.12.0
SampleQC	Macnair and Robinson ⁶⁴	v0.6.6
Harmony	Korsunsky et al. ¹⁶	v0.1.1
edgeR	Robinson et al. ⁶⁵	v4.0.2
ANCOM-BC	Lin and Peddada ⁶⁶	v2.2.2
miRoR	Dann et al. ²⁷	v2.2.0
glmmTMB	Brooks et al. ²⁸	v1.1.2.2
FGSEA	Korotkevich et al. ⁶⁷	v1.32.0
PAGA	Wolf et al. ¹⁹	Implemented within v1.9.4 of scanpy
MOFA+	Argelaguet et al. ³¹	v1.16.0
scITD	Mitchel et al. ³⁵	v1.0.4
glmnet	Friedman et al. ⁶⁸	v 4.1-8
Other		
interactive web browser to analyse cell type-specific expression levels of genes and transcriptomic changes in MS versus control tissue	This paper	https://malhotralab.shinyapps.io/MS_broad/ ; https://malhotralab.shinyapps.io/MS_fine/

EXPERIMENTAL MODEL AND STUDY PARTICIPANT DETAILS

Human tissue

Human tissue samples were obtained from the Netherlands Brain Bank (NBB), the MS UK tissue bank (UKTB) and the Edinburgh Brain Bank (EBB) via donor schemes with full ethical approval from respective brain banks (METc/2009/148 from Medical Ethical

Committee of the Amsterdam UMC, MREC/02/2/39 from UK Ethics Committee), and individual material transfer agreements between Roche and ABB, UKTB and EBB. We have complied with all relevant ethical regulations regarding the use of human postmortem tissue samples.

In the discovery dataset, we examined a total of 156 (127 MS and 29 controls) snap frozen brain tissue blocks obtained at autopsies from 54 MS patients and 26 controls. MS patients and controls were similarly matched for age and sex. Samples were from frontal, parietal or temporal regions, with cortical GM or underlying WM. For detailed donor information see [Data S2](#). As some brain banks only collect disease samples rather than controls, we inevitably have some differences in sample source with case-control status and different collection practices also impact age and PMI for the GM samples ([Table S1](#)). However, we have had to be pragmatic with these precious resources. For example, analyses of these variables in our differential expression and cell composition analyses found very few genes or cell types associated with age. The details of the relevant genes are included in [Data S5](#). We have added a statement to this effect in the limitations section.

METHOD DETAILS

Sample preparation and single nuclei RNA sequencing

Brain tissue characterization

Snap frozen tissue blocks from donors with GM lesions were provided by UKTB to Roche. Subpial GM lesions were determined using MBP and PLP staining by neuropathologists at Roche and confirmed by independent experts (Anna Williams, Roberta Magliozzi). Pathological staging of WM lesions from EBB and ABB donor samples was done at the respective brain banks. In the WM, de- and remyelinated lesions were identified by Luxol Fast Blue (LFB) staining and demyelinated lesions were grouped into active, chronic active and chronic inactive lesions with Oil red O staining to determine microglial activity.⁶⁹ Remyelinated lesions were defined as showing light staining on LFB, and presence of only a few non-activated microglia/macrophages which did not contain ingested MOG, PLP or MBP. Brain tissue specimens from the respective WM regions were shipped on dry ice to Roche and directly processed.

Nuclei isolation and single nuclei RNA sequencing

Nuclei were isolated from fresh-frozen 10 μ m sections, using Nuclei Pure Prep Nuclei Isolation Kit (Sigma Aldrich) with the following modifications. The regions of interest were macro-dissected with a scalpel blade, lysed in Nuclei Pure Lysis Solution with 0.1% Triton X, 1mM DTT and 0.4U/ul SUPERase-In™ RNase Inhibitor (ThermoFisher Scientific) freshly added before use, and homogenised with the help first of a 23G and then of a 29G syringe. Cold 1.8M Sucrose Cushion Solution, prepared immediately before use with the addition of 1mM DTT and 0.4U/ul RNase Inhibitor, was added to the suspensions before they were filtered through a 30 μ m strainer. The lysates were then carefully layered on top of 1.8M Sucrose Cushion Solution. Samples were centrifuged for 45min at 16000xg at 4°C. Pellets were re-suspended in Nuclei Storage Buffer with 0.4U/ul RNase Inhibitor, transferred in new Eppendorf tubes and centrifuged for 5min at 500xg at 4°C. Pellets were again re-suspended in Nuclei Storage Buffer with 0.4U/ul RNase Inhibitor, and centrifuged for 5 minutes at 500xg at 4°C. Finally, purified nuclei were re-suspended in Nuclei Storage Buffer with 0.4U/ul RNase Inhibitor, stained with trypan blue and counted using an automated cell counter (Countess II, Life technologies). A total of 12,000 estimated nuclei from each sample was loaded on the 10x Single Cell Next GEM G Chip. cDNA libraries have been prepared using the Chromium Single Cell 3' Library and Gel Bead v3.3 kit according to the manufacturer's instructions. cDNA libraries were sequenced using Illumina NovaSeq 6000 System and NovaSeq 6000 S2 Reagent Kit v1.5 (100 cycles), aiming at a sequencing depth of minimum 30K reads/nucleus.

Immunohistochemistry and analysis

FFPE sections (4 μ m) were deparaffinized in decreasing concentrations of ethanol, and antigen retrieval was performed in antigen unmasking solution (Vector Laboratories, H-3300) for 10 min in the microwave. Sections were incubated with autofluorescence eliminator reagent (Millipore, 2160) for 1 min and washed with TBS 0.001% Triton-X (wash buffer). Endogenous peroxidases were quenched with 3% H₂O₂ for 15 min at room temperature (RT), washed in wash buffer and blocked for 30 min at room temperature with PBS 0.5% Triton-X (TBS-T), 10% HIHS (blocking buffer). Primary antibody incubation was performed overnight at 4°C in blocking buffer. Sections were washed and incubated for 2hrs at RT with HRP-labelled secondary antibodies. Fluorophore reaction was performed using OPAL 570 and OPAL 650 reaction kits for 10 min at RT (Akoya Biosciences, FP1488001KT and FP1496001KT respectively, 1:500). Sections were counterstained using Hoechst (Thermo Fisher, 62249; 1:1,000), washed and mounted.

The following primary antibodies were used: mouse anti-CNP (Atlas, AMAb91072, 1:1,000, RRID:AB_2665789), rabbit anti-human GPR17 (Cayman Chemical, 10136, 1:100, RRID:AB_10613826), MBP (Rat anti MBP aa82-87 BioRad 1:300, RRID:AB_10886666), PLP (Mouse anti-Myelin Proteolipid Protein Antibody, CT, clone PLPC1 MAB388 Millipore, 1:200, RRID:AB_177623), MHCII (Dako 1:50, RRID:AB_2313661), MOG Z12 (inhouse clone 1:50⁷⁰). The following secondary antibodies were used: Vector Laboratories, rabbit-HRP IgG (MP-7401, Vector laboratories, RRID:AB_2336529), mouse-HRP IgG (MP-7402, Vector laboratories, RRID:AB_2336528).

For quantifications of GPR17 cell numbers, sections were co-labelled with GPR17 and CNP which was used to define demyelinated lesions. Sections were scanned using a VectraPolaris slide scanner and processed using Qupath⁷¹ and Fiji⁷² imaging software.

Within individual lesions, several regions of interest were selected randomly. These regions of interest were randomised using the Fiji randomization plugin and quantified completely blinded mixing samples from all conditions, regions and lesions.

In Situ Hybridization on brain tissue - RNAscope

The RNAscope™ 2.5 LS Assay Brown kit (322100) was used to detect target RNA expression in fresh frozen tissue sections (15µm). Sections were mounted on charged Superfrost® plus slides and baked at 60°C for 1 hr. Tissue was then fixed with 10% neutral buffered formalin (NBF) for 15 min at 4°C, and dehydrated through 50%, 70% and 100% EtOH (5 min for each concentration and twice for 100% EtOH) and air-dried for 5 min. Following pre-treatment, the RNAscope™ 2.5 LS Assay was carried out on the Bond RX (Leica Biosystems), involving hybridization of each RNAscope probe to the target RNA, followed by signal amplification steps. Detection was achieved using the chromogenic substrate provided in the kit, resulting in a brown precipitate at the site of the target RNA. RNAscope probes used were: HSP90AA1 (477068), HMGB1 (434638), LINGO1 (414838), CRYAB (426278), NAMPT (599318), CD44 (311278), CLIP1 (447298), CACNA1A (558588), SHISA9 (831608), A2M (532508), TGFBR2 (407948), SYK (422838).

High resolution brightfield images were captured using a Zeiss Axioscan slide scanner and analysed using both QuPath and ImageJ software. Three ROIs were created for each tissue section (width: 2200µm; height: 1750µm) and DAB (brown) channel isolated. ROIs were imported into ImageJ, thresholded and smoothed. RNA particles were then calculated within each ROI using the ‘analyse particles’ function within ImageJ to provide quantitative data. The mean RNA signalling over all three ROIs per sample was calculated.

QUANTIFICATION AND STATISTICAL ANALYSIS

See [Figure S13](#) for an overview of the analysis workflow.

Sample swap checks via genotyping

We genotyped all samples included in this study using the GSAv3 illumina CHIP. Genotypes were imputed using the Haplotype Reference Consortium (HRC) reference panel (version r1.1)⁷³ and lifted over to GRCh38. Genotype processing and quality control was performed using Plink v1.9.⁷⁴ SNPs with imputation score <0.4 or with missingness greater than 5% were excluded. We used MBV⁷⁵ to identify sample swaps. Briefly, MBV takes as input a VCF file containing the genotype data of the samples, as well as bam files containing the mapped single nuclei sequencing reads. MBV then reports the proportion of heterozygous and homozygous genotypes (for each individual in the VCF file) for which both alleles are captured by the sequencing reads in all bam files. Correct samples can then be identified as they should have a high proportion of concordant heterozygous and homozygous sites between the genotype data and the mapped sequencing reads. We identified and corrected 23 sample swaps; three further samples were excluded because they could not be matched to a genotype.

snRNAseq data processing and quality control

All samples were processed with Cell Ranger (v3.1.0), using the GRCh38 reference human genome and the ensembl Homo_sapiens GRCh38.96 reference annotation (modified to count intronic reads, and including genes with gene biotype protein_coding, lincRNA, antisense, and IG_* and TR_* genes). Ambient RNA contamination was removed via processing all samples with CellBender (v0.2.2), using the *raw_feature_bc_matrix.h5* output file from Cell Ranger as input, with *-total-droplets-included* set to 25000, *-expected-cells* set to the “Estimated Number of Cells” given in the *CellRanger metrics_summary.csv* output file, and other parameters set to defaults. Barcodes called as cells by CellBender, with the corresponding cleaned count matrices, were used for gene expression quantifications. We used *velocyto* (v0.17.17) on the *CellRanger* output to quantify intronic and exonic reads.

We identified doublets using *scDbtFinder* (v1.12.0), applied to each sample separately (*multiSampleMode* = “split”), with all other parameters default.⁶³ We used the score threshold determined from the data by *scDbtFinder*.

After removing doublets, we did quality control, primarily on the basis of percentage of exonic reads. We first removed nuclei with insufficient data to be worth including, requiring nuclei to have a minimum of 300 expressed genes, 500 UMI counts, and a maximum of 50% mitochondrial reads. We also excluded samples where an excessive proportion of input barcodes were called as cells by *CellBender*. Specifically, for each sample we calculated the proportion of droplets given >50% probability of being a cell by *CellBender*, applied the logit transform, calculated the median, and excluded any samples whose proportion was more than 3 MADs distant from the median. The result of this was to exclude 7 GM samples with >95% droplets called as cells, one GM sample with <3% droplets called as cells, and no WM samples. We then excluded any nuclei with greater than 75% exonic reads, or greater than 20% mitochondrial reads. After applying these filters, we then excluded any samples with <500 nuclei remaining. This resulted in 64 GM and 92 WM samples passing QC, comprising 632k nuclei across 156 samples.

Data integration and clustering

Data integration

Data integration was done with *Harmony* (v0.1.1), as implemented within the Seurat package. Mitochondrial genes (those starting with MT-) were excluded. The counts data were loaded into a Seurat object, then we applied the functions *NormalizeData*, *FindVariableFeatures*, *ScaleData*, *RunPCA* (with *n_dims* = 50), followed by *RunHarmony*, with *group.by.vars* set to “sample_id”

(i.e. integrating across samples); with the exception of *n_dims* for RunPCA, all parameters were set to default. To identify clusters at the broad celltype level, we ran FindNeighbours then FindClusters, with resolution set to 1.

Broad cell types were assigned to each cluster on the basis of known marker genes: *PLP1*, *MAG*, *MOG*, *OPALIN* (Oligodendrocytes), *PDGFRA*, *BCAN* (OPCs / COPS), *FGFR3*, *GFAP*, *SLC14A1*, *AQP4* (Astrocytes), *P2RY12*, *SPP1*, *CSF1R*, *IRF8* (Microglia), *SLC17A7*, *FEZF2*, *RORB* (Excitatory neurons), *GAD1*, *ADARB2*, *LHX6* (Inhibitory neurons), *CLDN5*, *FLT1*, *EPAS1* (Endothelial cells), *EPS8*, *LAMA2* (Pericytes), *IGHG1* (B cells) and *IL7R* (T cells). The log normalised expression of each gene was calculated for each cluster, and these values scaled to 0 to 1 over all clusters. For each cluster, the broad cell type with the highest scaled expression averaged over the known marker genes was selected as the label.

Subclustering

Integration with Harmony identified cell types annotated with broad cell type labels. To identify subclusters corresponding to cell states, we repeated the integration process within the broad cell types. It is not advisable to integrate samples with very small numbers of cells. To avoid this, we first grouped the broad cell types together into the following six combinations of cell types, with the number of PCs used given in brackets: OPCs + COPS and oligodendrocytes (30 PCs); astrocytes (20 PCs); microglia (20 PCs); excitatory neurons (30 PCs); inhibitory neurons (30 PCs); and endothelial cells, pericytes, T cells and B cells (20 PCs).

For each of these broad cell type groupings, even after grouping together, some samples had very low numbers of cells. We therefore excluded any samples with fewer than 100 cells before performing integration with Harmony. Harmony was performed as above, with resolution 0.2 for all broad cell type groups, except OPCs + COPS and oligodendrocytes where we used resolution 0.5. Any clusters with fewer than 200 cells in total were excluded.

To label the cells in the samples with fewer than 100 cells, we trained a classifier (XGBoost⁷⁶) on up to 1000 randomly selected cells from each cluster, using a second set of an equal number of randomly selected cells as a validation set. This classifier was applied to all unlabelled cells, and all cells that the classifier labelled with at least 50% probability were retained.

This resulted in 68 distinct batch-corrected fine cell type clusters, comprising: 11 of oligodendroglia; 7 of astrocyte; 7 of microglia / perivascular macrophages; 14 of cortical excitatory neurons (across layers 2-6); 12 of inhibitory neurons; 7 blood vessel-related cells (including 4 endothelial cell and 1 pericyte clusters); B cell and T cell subpopulations; and 9 clusters with mixed lineages. These mixed clusters could potentially be doublets that had not been identified by *scDbtFinder*, and were therefore excluded from further analysis; this resulted in 59 QC-passed clusters.

Independent data processing, integration and clustering

We additionally performed an entirely independent processing pipeline (distinct methods for: handling ambient RNA contamination; QC; integration; and clustering). We found high concordance between the clusters identified by both methods (Figure S2A; Data S3).

Marker gene identification and cell type annotation

To identify marker genes within each of the 6 broad cell type groupings, we used *edgeR* applied to pseudobulk counts of each sub-cluster in each sample. This avoids the inflated FDR values due to pseudoreplication that are common to methods such as FindMarkers in Seurat.¹⁵ To do this, we first constructed a matrix of pseudobulk values, where each row corresponds to a gene, and each column corresponds to the sum of all the cells of one cluster in one sample. We ran *edgeR* using *calcNormFactors* with the method “TMMwsp” applied to library sizes across all clusters simultaneously (the default here is “TMM”, however “TMMwsp” is designed to better take zeros into account, and is therefore more appropriate when some samples may have small library sizes). The cluster variable was used to construct the design matrix for estimating dispersions via *estimateDisp*. We then ran *glmQLFit* and *glmTreat* on each cluster, with the formula $\sim is_cluster$, where $is_cluster = cluster == sel_cl$, to identify genes that are differentially expressed in that cluster relative to all other clusters. We defined marker genes as genes differentially expressed in a cluster, not labelled as either lincRNA, pseudogene or antisense, with positive logFC, and ≥ 1 CPM mean expression in that cluster. We then ran FGSEA on the marker genes identified for each cluster, using logFC as the ranking variable.

Differential abundance of cell types in MS lesions and control samples - ANCOM-BC

We first checked for samples with sample sizes that were much smaller than for other samples, to exclude samples where abundances might be very noisy. We excluded samples with log sample sizes $2 * MAD$ (median absolute deviation) less than the median log sample size, separately for WM and GM; this excluded zero WM samples and two GM samples. We also checked for samples with unusual proportions of neuronal cells relative to other WM or GM samples. White matter samples with neuronal proportion at least $2 * MAD$ (median absolute deviation) higher than the median neuronal proportion for all WM samples were excluded; grey matter samples with at least $2 * MAD$ neuronal proportion fewer than the GM median neuronal proportion were excluded. This excluded 18 out of 94 WM samples and 1 out of 71 GM samples.

To test whether abundances of fine cell types across samples were affected by lesion type and donor ID (Figures 2I and 2J), we used likelihood ratio tests applied to models including lesion type and donor id. Briefly, we fit a series of nested models for each fine cell type: full ($counts \sim lesion_type + sex + age_scale + pmi_cat + (1 | donor_id)$), fixed ($counts \sim lesion_type + sex + age_scale + pmi_cat$), covariates only ($counts \sim sex + age_scale + pmi_cat$) and null ($counts \sim 1$). We used the R package *glmmTMB* (v1.1.2.2)²⁸ to fit a negative binomial distribution to the raw counts for each cell type (see supplemental information for explanation of use of raw counts rather than proportions). We used the function *anova* to perform likelihood ratio tests of the following nested sequence of models: full; fixed; covariates only; null. This gives a p-value indicating whether the more complex model improved the fit more than would be

expected by chance. We adjusted the p-values across these tests using the Benjamini-Hochberg procedure, across all cell types and models together.

To test for differential abundance in fine cell type due to lesion type, we used ANCOM-BC version 1.3.2.⁶⁶ The likelihood ratio test analysis above indicated that donor ID needed to be taken into account, however this version of ANCOM-BC does not allow random effects. To factor out donor effects, we therefore did a bootstrapped analysis of abundance: each bootstrap took one random sample per donor, and ran ANCOM-BC on each bootstrapped sample (e.g. in WM, there were 76 samples across 42 donors, so each bootstrap comprised 42 samples). We summarised the results of 20k bootstraps by taking the median, 80% and 95% confidence intervals of the inferred coefficients for each fine cell type (20k samples is sufficient to properly estimate tail probabilities for 95% CIs; cf Hesterberg 2011⁷⁷).

To test differential abundance in WM samples, we additionally excluded all neuronal cell types, as these should not be present in WM. We fit ANCOM-BC with the formula $\sim lesion_type + sex + age_scale + pmi_cat$, where *age_scale* is patient age, scaled to have SD = 0.5 across all patients in the dataset,¹² and *pmi_cat* is post-mortem interval, split into three categories (under 1 hour, between 1 and 12 hours, and more than 12 hours).

To test differential abundance in GM samples, we first fit the data with a similar formula: $\sim lesion_type + sex + age_scale + pmi_cat2$ (here, *lesion_type* includes ctrGM, NAGM and GML; *pmi_cat2* has only two categories to reflect the values observed in GM, between 1 and 12 hours, and more than 12 hours).

Using this formula this produced results that conflicted with known biology, identifying multiple neurons as increasing in abundance in GM lesions relative to GM controls. Analysing differences between neuronal proportions between ctrGM, NAGM and GML, we observed that GML samples were enriched in L1/L2/L3 neurons, and those from NAGM samples were enriched in L5/L6 neurons (ctrGM samples had intermediate proportions) (Figure S12A). This indicated that GML samples were taken from more superficial cortical layers in the brain, and the matched NAGM also contained deeper layers (although the experimenters had made efforts to take all samples from the same depth).

To identify layer effects for each sample, we calculated principal components (PCs) reflecting neuronal layer distributions in normal tissue. We applied PCA to the centred log ratios of the neuronal cell types in the control GM samples. We then identified principal components that could be relevant to layers (by filtering on both the absolute Spearman rank correlation between the PC loading and the layer numbers of neurons known to be layer-specific, thresholding at minimum 0.2 correlation) and which explained at least 1% of variance. This identified seven PCs that could contain layer information (Figure S12B). This analysis was performed in control GM samples only; we then calculated CLR for all samples, and projected them into the selected PCs, using the loadings derived from the control samples.

We then repeated the bootstrapped ANCOM-BC analysis, including layer PCs as covariates to factor out layer effects. We used the formula $\sim lesion_type + sex + age_scale + pmi_cat2 + layerPC1 + \dots + layerPCn$, i.e. we repeated the analysis using the first *n* layer PCs identified above, including from 1 up to 7 PCs. We found that including the first 3 layer PCs gave results that fitted well with expected biology, i.e. that almost no neuronal types were found to increase in abundance in either NAGM or GML relative to control GM, and PVALB+ neurons decreased in abundance (Figures S12C and S12D). We included 3 layer PCs, however there is little difference in the results for including between 3 and 7 layer PCs.

Differential abundance of cell types in MS lesions and control samples – *miloR*

miloR is an R package that identifies neighbourhoods within a nearest neighbours graph that are enriched or depleted in cells from a particular condition.²⁷ We ran *Milo* on WM and GM samples separately, using a graph constructed on Harmony-corrected principal components.

Briefly, we restricted to relevant cell types for each tissue (WM: OPCs + COPs, Oligodendrocytes, Astrocytes, Microglia, T cells, B cells; GM: OPCs + COPs, Oligodendrocytes, Astrocytes, Microglia, Excitatory neurons, Inhibitory neurons, T cells, B cells), and selected 2000 highly variable genes evenly across each major cell type (this ensures that the HVGs are not dominated by the cell types with largest numbers). We then ran Harmony on the selected cells and HVGs using the default parameters.

To account for multiple samples per donor, we did a bootstrapped analysis of abundance, as with ANCOM-BC: each bootstrap took one random sample per donor, and ran *miloR* on each bootstrapped sample. (The bootstrapping was only of the counts of cells, and not of the graph construction.) We performed 2000 bootstrap replicates for each model tested.

To identify the neighbourhoods associated with lesion types, we applied the bootstrapped *miloR* with the following formulae: WM, $\sim lesion_type + sex + age_scale + pmi_cat$; GM, $\sim lesion_type + sex + age_scale + pmi_cat2 + ctrl_PC01 + ctrl_PC03 + ctrl_PC04$. The 3 layer PCs here are to correct for layer effects in the GM tissue, as described in the ANCOM-BC analysis. To identify the neighbourhoods associated with factors, we applied the bootstrapped *MiloR* with the following formulae: WM, $\sim WM_F1 + WM_F2 + WM_F3 + WM_F4 + WM_F5 + sex + age_scale + pmi_cat$; GM, $\sim GM_F1 + GM_F2 + GM_F3 + GM_F4 + GM_F5 + sex + age_scale + pmi_cat2 + ctrl_PC01 + ctrl_PC03 + ctrl_PC04$.

To plot the bootstrap results, we showed the median bootstrap value per neighbourhood. We reported the coefficient for a neighbourhood as being significantly different from zero if the 90% bootstrap interval of the log₂FC did not overlap with the interval $[-\log_2(1.2), \log_2(1.2)]$ (this is the same principle as in the *TREAT* method in *edgeR*⁷⁸). We used the function *annotateNhoods* in *miloR* to give fine cell type labels to each neighbourhood.

Differential expression analysis using generalised linear mixed models

To identify genes differentially expressed in MS WM and MS GM samples compared to respective control samples per cell type, we did differential expression analysis on pseudo-bulk data, i.e. analysis at the level of the transcript totals across all cells of a given type in each sample. Pseudobulk approaches are known to offer a good compromise between sensitivity and run time constraints^{79,80} (see [supplemental information](#) for the details of our analysis using different pseudobulk approaches and identification of strong patient effects). Inspection of gene expression at the donor level indicated that our model would need to include donor effects.

We therefore used `glmmTMB`²⁸ with a negative binomial model, and *donor_id* as a random intercept. To filter out samples with low library sizes or numbers of cells, genes with low counts, and estimate library sizes, we followed the approach set out in *muscat*.⁷⁹ Briefly, this comprises: removing samples with fewer than 10 cells; removing pseudobulk samples whose log library size is less than 3 MADs less than the median; removing genes with low expression using the function *filterByExpr* in *edgeR*; calculating TMM-normalised library sizes with the function *calcNormFactors* in *edgeR*.⁶⁵

The formula for WM was $counts \sim lesion_type + sex + age_scale + pmi_cat + (1 | donor_id)$, where *pmi_cat* is post-mortem interval, split into three categories (under 1 hour, between 1 and 12 hours, and more than 12 hours, and *age_scale* is patient age, normalised to have $SD = 0.5$).¹²

In the GM analysis, we accounted for layer effects by including 3 layer PCs as described in the ANCOM-BC analysis. The formula for GM was therefore $counts \sim lesion_type + sex + age_scale + pmi_cat2 + ctrl_PC01 + ctrl_PC02 + ctrl_PC03 + ctrl_PC04 + (1 | donor_id)$; to reflect values observed in GM samples, *pmi_cat2* has only two categories (between 1 and 12 hours, and more than 12 hours). We included an offset of $\log(lib.size) - \log(1e6)$, so that the reported coefficients correspond to log counts per million (logCPM). Genes with absolute \log_2 fold change in expression of at least $\log_2(1.5)$ and an FDR-corrected $P < 0.05$ were selected as differentially expressed. FDRs were calculated at the level of combination of cell type and model coefficient.

To quantify the extent of donor effects, for each gene we also used `glmmTMB` to fit three simpler models (in addition to the full model with all variables): with lesion type plus covariates (i.e. fixed effects only) ($counts \sim lesion_type + sex + age_scale + pmi_cat$), with covariates only ($counts \sim sex + age_scale + pmi_cat$) and a null model ($counts \sim 1$). We then used the `anova` function to perform likelihood ratio tests for this nested sequence of models; we applied a Benjamini-Hochberg correction across all genes and LRTs, separately within each cell type.

Gene set enrichment analysis of differentially expressed genes

FGSEA⁶⁷ was used to perform statistical enrichment tests of differentially expressed genes in each cell type (broad and fine) from each comparison in WM and GM samples. All genes expressed in a given cluster were used as a background list, and GO-term analysis for enriched biological processes and hallmark genes from MSigDB⁸¹ was performed. Z-score was used as the ranking variable in FGSEA (calculated from the unadjusted p-value and the sign of the log fold change). FDR correction was calculated within each combination of cell type, model coefficient and pathway collection. Processes with an FDR-corrected $P < 0.1$ were considered and their normalised enrichment scores (NES) plotted as a dotplot using `ggplot2`⁸² R-based libraries.

Assessment of cluster connectivity with PAGA

To characterise connectivity between clusters, we used PAGA¹⁹ as implemented in `scanpy` version 1.8.2.⁸³ As input, we used the nearest neighbour graph constructed by `conos`, restricted to just cells with oligodendrocyte or OPC / COP labels. We ran PAGA clustering and layout embedding using fine cell types as the group variable, and otherwise used defaults.

Patient stratification using MOFA+

We used MOFA+ to identify factors explaining the variability across the samples (implemented in the R package MOFA2).³¹ MOFA+ was developed for data with multiple modalities measured from the same samples. In this study, we took the different *cell types* to be the different modalities. This allows us to identify responses that are coherent across samples, across multiple cell types simultaneously, and which may have cell type-specific responses. MOFA+ does this by finding factors that seek to explain the variability in the input data (intuitively similar to PCA) across samples, and which correspond to coordinated tissue-level responses, even though the genes identified for each cell type are distinct. For example, a factor corresponding to remyelination might involve myelination genes in oligodendrocytes, debris-clearance genes in microglia, and metabolic support genes in astrocytes. These factors can then suggest possible ways to stratify patients.

We first identified genes with relevant variation for each cell type, based on the negative binomial models fitted to each gene in each cell type. We identified genes with either an MS effect, or a donor effect (or both). Genes with an *MS effect* were defined as those where at least one lesion type had both an $FDR < 1\%$ and an absolute \log_2 fold change of 1 for WM, or $\log_2(1.5)$ for GM (we observed lower effect sizes in GM, and therefore used a more relaxed threshold). Genes with a *donor effect* were those where the likelihood ratio test of including the donor effect had an $FDR < 1\%$, and the standard deviation of the donor random intercepts was at least $\log(2)$ for WM, and $\log(1.5)$ for GM. These thresholds are arbitrary but we have found the factors identified by MOFA+ to be robust to variations on these thresholds. In WM, this resulted in the selection of: 231 genes for OPCs + COPs, 821 for oligodendrocytes, 1192 for astrocytes, 1023 for microglia, 225 for endothelial cells and pericytes. In GM, we selected: 339 genes for OPCs + COPs, 1039 for oligodendrocytes, 1239 for astrocytes, 412 for microglia, 1159 for excitatory neurons, 924 for inhibitory neurons, 852 for endothelial cells and pericytes.

We then calculated normalised expression for the selected genes in each cell type as input to MOFA+. We first excluded any samples with fewer than 10 cells observed for that cell type (this means that there may be missing data for some cell types in some samples). We also excluded any samples with log library sizes $3 \times \text{MAD}$ (median absolute deviation) less than the median log library size for that cell type. For the remaining samples, we calculated the $\log(\text{CPM} + 1)$ of the pseudobulk values, calculating CPMs with library sizes via the `effectiveLibSizes` function in `edgeR`.⁶⁵ To remove any possible layer effects in GM samples, we fit a linear model using the first four layer PCs as covariates, i.e. $\log\text{CPM} \sim \text{layerPC1} + \text{layerPC2} + \text{layerPC3} + \text{layerPC4}$, and used the residuals of this model as values for input to MOFA+. To ensure each gene contributed equally to the model, we then z-scored all resulting values within each combination of gene and cell type.

For each of WM and GM, we then fit MOFA+ to this data, using 5 factors. As we are interested in an unbiased characterisation of the heterogeneity of the data, we did not use the group variable in MOFA+; otherwise we used the default parameters. In both WM and GM, we found 5 factors which explained at least 5% of variance for some cell type.

As described above, we fit MOFA+ only to a relevant subset of genes for each cell type. To identify associations between the identified factors and all genes, we then used `edgeR` fit to the counts of each gene, with the formula $\sim \text{WM_F1} + \text{WM_F2} + \text{WM_F3} + \text{WM_F4} + \text{WM_F5} + \text{sex} + \text{age_scale} + \text{pmi_cat}$ (and similarly for GM).

To estimate the variance explained by the MOFA factors across all genes, we first obtained variance-stabilised log transforms of the data with the `vst` function in the R package `DESeq2`⁸⁴; notably, this shrinks the high sampling variability of genes with low mean counts. We then fit a linear model to the log-transformed values of each gene with the formula above, calculated `anova`, and recorded the sum of squares for each factor. We restricted to genes with `vst`-transformed variance of at least 0.5, and calculated variance explained as the total sum of squares for each factor, divided by the total variance across all included genes.

To calculate geneset enrichment of the genes in MOFA+ factors, we ranked the genes for a given cell type in descending order of the signed log `edgeR` p-value, and used the function `fgseaMultilevel` from the FGSEA package,⁶⁷ using a minimum set size of 5 genes and otherwise the default parameters.

Validation of MOFA+ factors with scITD

scITD is a computational method designed to extract multicellular gene expression programs that vary across donors or samples.³⁵ We ran scITD on WM pseudobulk data from the same set of cell types used as input to MOFA (i.e. OPCs + COPs, oligodendrocytes, astrocytes, microglia, endothelial cells and pericytes). We used the parameters set out in the method vignette (<http://pklab.med.harvard.edu/jonathan/>), resulting in inclusion of 5098 genes across all cell types.

Projection of MOFA+ factors onto new cohort

To estimate factor values on the second cohort, we used a regularised regression model trained on the first cohort, and applied it to the second cohort. The regression task was to predict a factor score for each sample, using as predictors a matrix of gene expression for different genes in each celltype, with all celltypes concatenated together.

To train the regression model, we used log CPM pseudobulk expression values for each gene in each celltype as variables, for the five broad celltypes used in the WM MOFA model: Oligodendrocytes, OPCs + COPs, Astrocytes, Microglia, Endo + Peri. CPM values were calculated using TMM-normalised library sizes. Within each celltype, genes were filtered by the median absolute deviation of the logCPM values, with a minimum MAD of 1 required. This resulted in 592, 387, 1710, 939 and 1995 genes being kept respectively for the celltypes in the order listed previously; this resulted in a total of 5623 distinct *celltype*gene* combinations. Each gene was then scaled to have mean 0 and sd 1. The input to the regression model was a matrix of 5623 *celltype*gene* combinations, across 92 WM samples. We used the function `cv.glmnet` from the package `glmnet` (v 4.1.8), with the parameter `alpha` set to 1 to give ridge regression. To define the folds for cross-validation, we split the donors in the Cohort I white matter data into 5 folds, distributing donors with larger numbers of samples evenly across folds. We trained a separate model for predicting each factor separately, and chose the model corresponding to `lambda.min` to minimise error. This resulted in 77, 75, 74, 95 and 78 *celltype*gene* combinations with non-zero coefficients for factors 1 to 5 respectively.

To predict the MOFA values in Cohort II, we scaled the logCPM values for the 5 celltypes by the mean and sd calculated from the samples in Cohort I. We then multiplied these values by the coefficients calculated by the regression model. As a sanity check, we also calculated these estimated factor values for the samples in Cohort I, and checked that they correlated extremely closely with the original values used for training.

Selection of probes for validation of MOFA+ factors by in situ hybridisation on tissue

We summed transcripts across all cell types for each sample, to create approximations to bulk samples and used a standard `edgeR`⁶⁵ analysis pipeline to identify genes that were significantly associated with each MOFA factor in the WM samples. To identify candidate biomarkers, we filtered for genes that were significantly up-regulated with a minimum level of expression ($FDR < 0.05$; $\log_{2}FC > 0$; $\log_{2}CPM > \log_{2}(50)$), annotated them as being secreted or not in the Human Protein Atlas^{85,86} (proteintlas.org) and prioritised those with high expression as these would be more likely to be detectable by in situ hybridization techniques. Note that the genes that are significantly associated with factors can differ at the bulk level from the pseudobulk (i.e. individual cell type) level, as the bulk level reflects changes in expression within cell types, *multiplied by* changes in proportions of cell types.

Contribution of model elements to cell type abundance variability

To test whether lesion type and donor ID explain the cell type proportion across samples, we fit a series of nested models of increasing complexity for each cell type:

- null ($counts \sim 1$);
- covariates only full ($counts \sim sex + age_norm + pmi_cat$);
- fixed full ($counts \sim lesion_type + sex + age_norm + pmi_cat$); and
- full ($counts \sim lesion_type + sex + age_norm + pmi_cat + (1 | donor_id)$).

We use the R package *glmmTMB* (v1.1.2.2) to fit a negative binomial distribution for each model to the raw counts. We then use likelihood ratio tests (via the *anova* function) to test whether the more complex model increases the goodness of fit, i.e. whether adding this variable improves the model more than we would expect by chance. We adjusted the p-values across these tests for all cell types using the Benjamini-Hochberg procedure (i.e. across $3 * 50$ p-values).

Note that we model raw counts rather than cell type proportions. An implicit assumption here is that there is no consistent bias in sample sizes between conditions or donors. This is a strong assumption, however this analysis is used only to make a weak conclusion, that donor variability is an important factor for some cell types.

If we model cell type proportions rather than raw counts, we introduce difficulties due composition (i.e. proportions summing to 1). Here, an increase in the proportion of one cell type results in a decrease in the proportion of all other cell types. Treating the data as compositional makes interpretation much more challenging, as differences in proportion could equally be caused by an increase in absolute abundance of one cell type, or a decrease in absolute abundance of a different cell type. In particular, it makes it difficult to make conclusions such as “abundance of cell type A varies considerably between MS patients”, as this apparent effect may be mediated by another cell type. The true explanation could be “abundance of cell type B varies considerably between MS patients; this results in high patient-patient variability in the proportion of cell type A”.

Differential abundance of cell types in MS lesions and control samples

Differential abundance involves testing whether the abundance of a given group changes consistently between conditions; in our case, this indicates whether particular cell types are enriched or reduced in MS lesions vs controls. Such tests are subtle: to account for experimental variability, we would like to normalise by the total number of cells, and work with proportions. However, in the case where one cell type increases in abundance and all other cell types remain unchanged, the proportions of the other cell types will decrease, and vice versa.

Various methods have been developed to address this point. They principally use one or more cell types whose abundance is assumed to remain unchanged between all samples, and can therefore be used as a reference. ANCOM-BC is a method developed for microbiome data that uses a mixture model to computationally identify cell types which remain unchanged, and does not require users to specify a reference cell type.⁶⁶ An independent benchmarking study (of microbiome data) found ANCOM-BC to consistently be one of the best-performing currently available methods.⁸⁷ scCODA is a method developed specifically for single cell data, however it requires users to specify one unchanging cell type as reference⁸⁸. As we do not know *a priori* which cell types are unaffected by MS, we used ANCOM-BC, and were unable to cross-check the results against scCODA.

Differential expression analysis using generalised linear mixed models

Recent work has indicated that the primary limitation in differential expression analysis is sampling from a small number of individuals,^{80,89} and that pseudo-bulk approaches such as Muscat⁷⁹ (that work at the level of the transcript totals across all cells of a given type in each sample) offer a good compromise between sensitivity and run time constraints. We therefore considered several pseudo-bulk approaches for analysing differential expression between our comparisons of interest. After analysis of the options, we chose a negative binomial model with a random effect, fit to count data with the *glmmTMB* package.²⁸

Initially, we ran muscat with edgeR,⁶⁵ using the formula $counts \sim lesion_type + sex + age_scale + pmi_cat$. Here, *age_scale* is patient age, normalised to have SD = 0.5,¹² and *pmi_cat* is post-mortem interval, split into three categories (under 1 hour, between 1 and 12 hours, and more than 12 hours). However, we found that for some genes there were substantial patient effects, i.e. genes where the donor ID was a much stronger determinant of expression than lesion type. Unfortunately edgeR does not at present allow random effects models.

We then investigated using dream from the variancePartition package,⁹⁰ however we found that it returned extremely low numbers of results for cell types where the library sizes were low. In particular, this resulted in 2 significant results being reported for immune cells, compared to over 200 (biologically expected) genes reported for the same comparison with the negative binomial model. This may be due to dream operating on logCPM values, which do not explicitly model the variability of small counts. Using a mixed model also has the advantage of returning a value for each donor random effect (i.e. donor) in the study, which can be interesting for downstream analysis.

We therefore used a generalised linear mixed model, to allow both random effects and properly model count data. We used the *glmmTMB* function from the *glmmTMB* package,²⁸ with a negative binomial model, and *donor_id* as a random effect. The formula for

WM was $counts \sim lesion_type + sex + age_scale + pmi_cat + (1 | donor_id)$; the formula for GM was $counts \sim lesion_type + sex + age_scale + pmi_cat2 + (1 | donor_id)$, where *pmi_cat2* has only two categories (between 1 and 12 hours, and more than 12 hours). We included an offset of $\log(lib.size) - \log(1e6)$, so that the reported coefficients correspond to log counts per million (logCPM).

For a small number of genes, there were zero counts for the control condition. Where this occurs, glmmTMB does not fit properly (it operates at the log scale, and such a situation corresponds to the mean of one condition equalling $\log(0)$, i.e. minus infinity). Where an all-zeros condition occurred, we therefore added a count of 1 to the sample in the all-zeros condition with the largest library size. This is the smallest possible perturbation that avoids complete separation of the data.

Statistical analysis

No statistical methods were used to predetermine sample sizes, but our sample size is eight times larger than those reported in previous snRNAseq MS publications (Jäkel et al.,⁷ Schirmer et al.,⁸ Absinta et al.⁹). Statistical analyses and graphical visualisations were performed using open-source R programming software.⁹¹ See dedicated method sections for the details of the snRNA-seq bioinformatic analysis; differentially expressed genes were defined as genes significantly expressed (*P* adjusted for multiple comparisons < 0.05), and showing, on average, >1.5-fold difference between groups of nuclei in each cell type in every DEG comparison. Volcano plots were constructed by plotting the \log_2 (fold change) of lesion type with smallest p-value for each gene in the x axis and by plotting standard deviation of random (donor) effects for each gene on the y-axis. Statistical analysis used two tailed parametric or non-parametric t-tests for two groups, and Fisher's exact test and one-way analysis of variance with corresponding post hoc tests for multiple group comparisons. Data distributions are presented as barplots, dotplots (with individual data points) and heatmaps. Log CPM gene expression values in the dot plots and heat maps were averaged, mean-centred, and z-score-scaled. Dot size indicates the percentage of nuclei in the cluster in which the gene was detected; among the nuclei in which the gene was detected, the expression level was mean-centred and scaled. Graphical object in [Figure 1A](#) was created with [BioRender.com](#).

ADDITIONAL RESOURCES

Two interactive web browsers for analysing cell type-specific expression levels of genes and transcriptomic changes in MS versus control tissue are available:

- At broad celltype level: https://malhotralab.shinyapps.io/MS_broad/
- At fine celltype level: https://malhotralab.shinyapps.io/MS_fine/